

CHAPTER-5

Electrical Properties

In this chapter we present results and discussion of the impedance spectroscopy carried out on the electrolyte system.

5.1 Ionic Conductivity

Electrochemical impedance spectroscopy EIS, is a perturbative characterization tool employed to understand complex mechanism of electrochemical processes.

Electrochemical impedance is usually measured by applying AC signal across an electrochemical cell and recording the current response through the cell. Measured impedance spectra when fitted with equivalent circuit model, represent an electrical identity of the sample yielding important information about the electrical properties of the sample (*Grossi and Riccò, 2017*). For small AC excitations, a pseudo-linear response of an electrochemical cell results in characteristic phase shifts as depicted in **Fig. 5.1**.

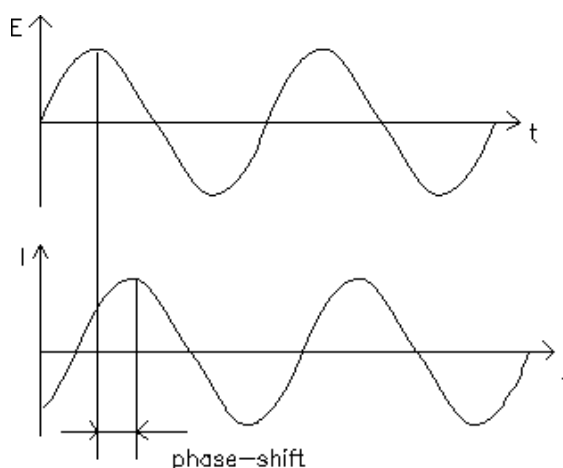


Fig. 5.1 Sinusoidal Current response in a linear system.

<https://www.gamry.com/application-notes/EIS/basics-of-electrochemical-impedance-spectroscopy/>

The input, $E(t) = E_0 \sin(\omega t)$ gives a phase shifted output of, $I(t) = I_0 \sin(\omega t + \varphi)$.

Using ohm's law to express it we have

$$Z = \frac{E(t)}{I(t)} = \frac{E_0}{I_0} \left(\frac{\sin(\omega t)}{\sin(\omega t + \varphi)} \right) = Z_0 \left(\frac{\sin(\omega t)}{\sin(\omega t + \varphi)} \right) \quad (5.1)$$

Using Euler's relationship, $\exp(j\varphi) = \cos\varphi + j\sin\varphi$, the impedance is represented in a complex function as, $Z(\omega) = Z_0(\cos\varphi + j\sin\varphi)$. Nyquist plot is used to represent this complex impedance graphically in a more feasibly interpretable form. On the Nyquist Plot, the impedance can be represented as a vector (arrow) of length $|Z|$. The angle between this vector and the X-axis, commonly called the "phase angle", is $f(=arg Z)$. Nyquist diagrams are interpreted using equivalent electrical circuit model.

Dielectric and modulus formalisms are used as other powerful approaches to have a closer understanding of electrical relaxation processes occurring in frequency domain of various types of solids. Complex impedance Z^* mechanism is used to extract dielectric $\varepsilon^*(\omega)$ and modulus M^* formalisms.

In the present chapter, conduction mechanism occurring inside ionically conducting material is characterized and distinguished by impedance, dielectric permittivity and electrical modulus. Conductivity as a function of temperature, composition, fluence and frequency is discussed in detail using impedance analysis. Relaxation processes are studied using dielectric and modulus formalisms. Electrical properties of prepared blend electrolyte system are measured from ambient to 333 K, in the frequency range from 20 Hz to 2 MHz. Following given systems of blend polymer electrolyte (BPE) systems were prepared for studying the conduction mechanism and we shall discuss about them one after the other.

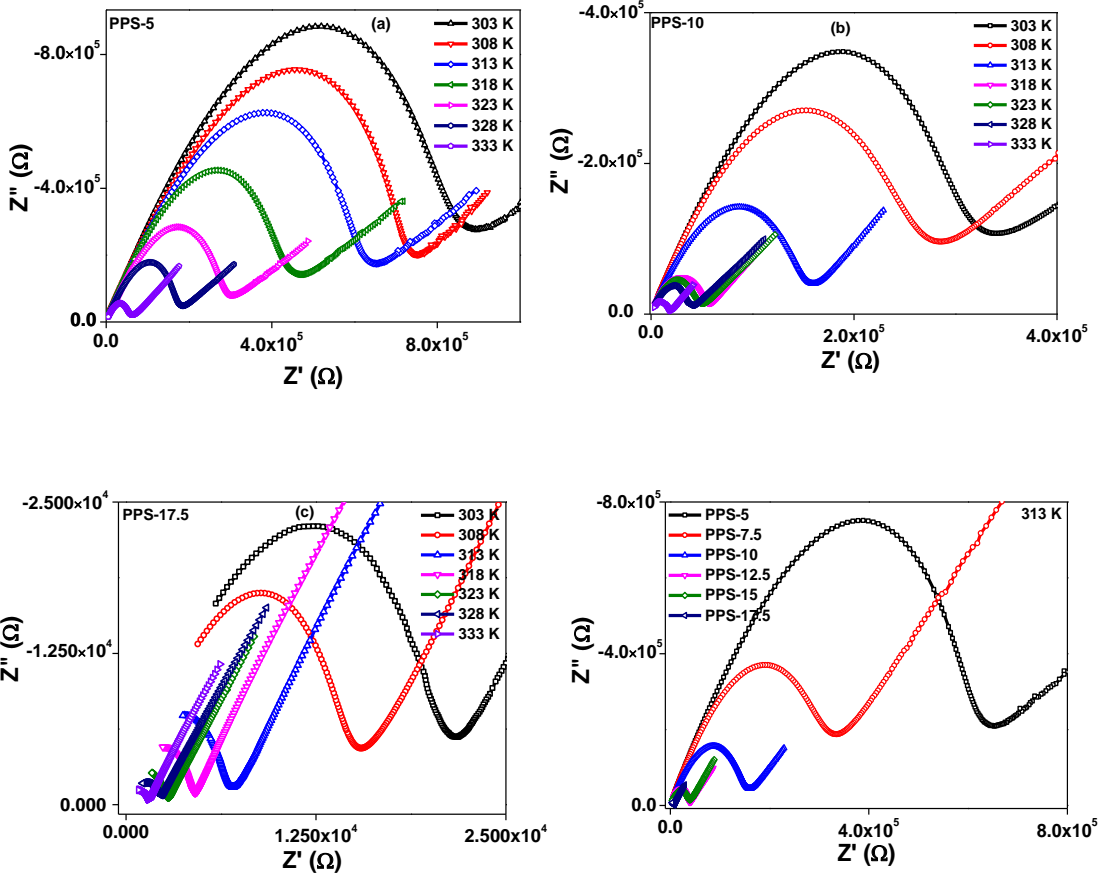
1. First system (PPS – system) Blend electrolytes are prepared as 1: 1 (w/w) (PEO – PAM) + x wt% NaCF_3SO_3 $x = 5$ wt% - 17.5 wt% in steps of 2.5
2. Second system (PPSP – system) plasticized blend electrolytes are prepared as 1: 1 (w/w) (PEO – PAM)– 12.5 wt% NaCF_3SO_3 + x wt% 1: 1 (w/w) (EC-PC) $x = 5$ wt% - 25 wt% in steps of 5
3. Third system (PPSPN – system) plasticized nano-composite blend electrolytes are prepared as 1: 1 (w/w) (PEO – PAM) – 12.5 wt% NaCF_3SO_3 – 20 wt% (EC – PC) + x wt% SiO_2 $x = 5$ wt% -15 wt% in steps of 2.5

All the three systems were then subjected to irradiation with 80 MeV swift heavy O^{6+} ion beam at four different fluences of 1×10^{11} , 3×10^{11} , 1×10^{12} and 2×10^{12} ions/cm². We shall also discuss conductivity behaviour, dielectric properties and modulus formalism in the un-irradiated samples as well as irradiated one to understand the effect of irradiation with 80 MeV swift heavy O^{6+} ion beam.

Effect of NaCF₃SO₃ on ionic conductivity

Impedance plots for various concentrations of NaCF₃SO₃ in PPS system recorded at different temperatures are shown in Figs. 5.2(a-c). Typical semi-circle in the plots indicate partial resistive-capacitive nature of electrolytes. Intercept of the semi-circle on the X-axis gives the value of bulk resistance R_b . It is observed that the intercept shifts towards the origin i.e., the bulk resistance decreases with increase in temperature for all the blend electrolyte samples. Impedance plots of PPS system at 313 K is shown in Fig. 5.3. It is observed that the value of bulk resistance R_b decreases continuously from 5 wt% to 17.5 wt% NaCF₃SO₃ content. Equivalent circuit model used to fit the impedance plots in PPS system is shown in Fig. 5.4.

Randles (1947) suggested that, to understand the process of electrolyte reactions, one must take into account the rate of control due to combined influence of electrode process and diffusion and devised the following model popularly known as **Randles cell** (Fig. 5.5). The resistance R_I in Fig. 5.4 below is basically R_e (electrolyte resistance) given as $R_e = \rho \frac{l}{A}$, (ρ : solution resistivity, A : bounded area where current is carried and l : length carrying uniform current), which depends on factors such as ion type, ion concentration, temperature and geometry of current carrying area. Generally, most electrochemical cells do not have a uniform current distribution over definite area and hence the resistance can be practically calculated using Charge Transfer Resistance value R_{ct} (shown in Fig. 5.5 as R_2 and popularly known as the bulk resistance R_b) $R_{ct} = \frac{RT}{nF i_0}$ where i_0 : exchange current density, F : Faradays constant, T : temperature, R : gas constant and n : number of ions involved. R_{ct} involves transfer of ions across the double layer and is directly affected by the electrode potential. In an electrochemical cell, electric double layer (C_{dl}) exists at the electrode-electrolyte interface due to absorption of ions on the electrode surface, hence capacitors in the cell do not behave ideally and are instead present as Constant Phase Element (**CPE**). $Z_{CPE} = \frac{1}{(j\omega)^\alpha Y_0}$ where Y_0 : capacitance and α is the exponent which is generally <1 for electrochemical cell. Diffusion or (Warburg Impedance Z_w) is frequency dependent element. $Z_w = \sigma \left(\omega^{-\frac{1}{2}} \right) (1 - j)$ Z_w is low at high frequency values and increases at lower frequencies. Fig. 5.5 represents physical presence of all the elements of the Randles' cell.



Figs. 5.2(a-c) Impedance plots for various concentrations of NaCF_3SO_3 in PPS system recorded at different temperatures.

Fig. 5.3 Impedance plot of PPS-system at 313 K.

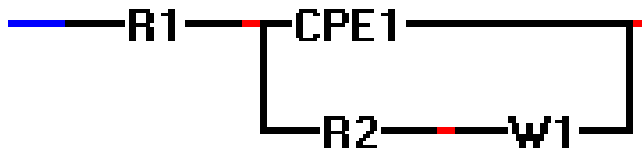


Fig. 5.4 Equivalent circuit model used to fit impedance data in PPS-system.

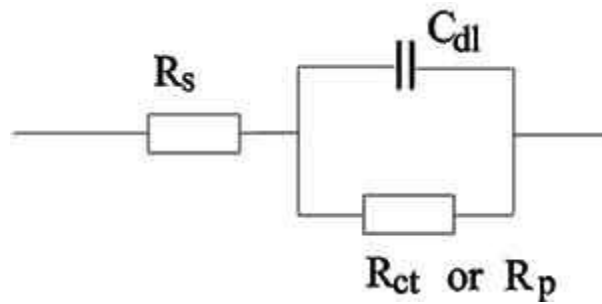


Fig. 5.5 A typical Randles cell model.

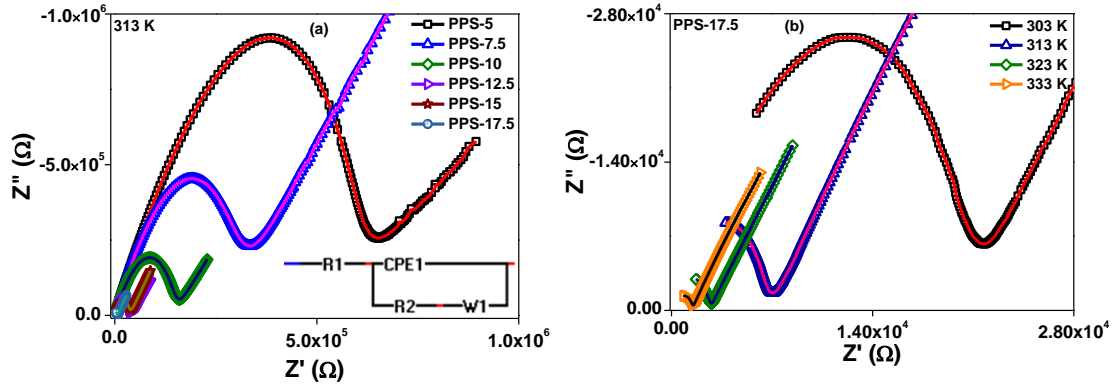


Fig. 5.6(a) Fitted impedance plot of PPS-system at 313 K and **(b)** Fitted impedance plot of PPS-17.5 sample at various temperatures.

Fitted impedance plot of PPS system at 313 K is shown in Fig. 5.6(a) and Fig. 5.6(b) shows fitted impedance plot of PPS-17.5 sample at various temperatures.

Measured values of R_b in each of the above cases is used to calculate the ionic conductivity of PPS system using the following equation

$$\sigma = \frac{l}{A} \times \frac{1}{R_b} \quad (5.2)$$

where l is the thickness of the sample and A is the area of the electrodes used. Variation in conductivity as a function of salt concentration is plotted in Fig. 5.7. The conductivity increases continuously with increase in amount of NaCF_3SO_3 from 5 wt% - 17.5 wt%. Maximum conductivity at room temperature is recorded to be $2.28 \times 10^{-6} \text{ Scm}^{-1}$ for PPS-17.5 sample. Increase in NaCF_3SO_3 concentration increases ionic dissociation in the system, a greater number of free ions are available for conduction and hence an increase in conductivity is noted. When the concentration of salt exceeds a certain optimal amount, re-association of ions takes place instead of dissociation and this leads to a decrease in the conductivity (Michalek et al., 2016; Imperiyka et al., 2013; Noto et al., 2011; Golodnitsky et al., 2009). But this is not true in the present case even after adding large amount (17.5 wt%) of NaCF_3SO_3 and we have thus optimised our PPS system at 17.5 wt% NaCF_3SO_3 concentration. Temperature response of conductivity of electrolyte samples of PPS system is plotted in Fig. 5.8. The plot of $\log \sigma$ vs. $1000/T$ is evidently not a straight line according to Arrhenius relation. The typical curvature behavior of the plots can be explained by VTF relation which indicates that the ion conduction strongly depends on polymer segmental motion. The VTF relation is given as follows.

$$\sigma = AT^{(-1/2)} \left(-\frac{B}{K(T-T_0)} \right) \quad (5.3)$$

where A is pre-exponential factor, $B = E_h + E_j + \frac{\omega}{2\epsilon}$ is the apparent activation energy associated with the hybrid energy which considers the ionic jump E_j , dissociation energy $\frac{\omega}{2\epsilon}$ and energy of hole formation E_h (opposing internal and external pressure to produce a hole responsible for ionic transport), K is the Boltzmann constant, T_0 is the ideal glass transition temperature, typically taken to be 50 K below T_g (Nava et al., 2016; Lian et al., 2014; Itoh et al., 2013). Increase in temperature leads to faster polymer chain relaxation which produces segmental motion (Khair et al., 2010), leading to an increase in the free volume of the system. Increase in free volume, favours ion movement which results in increase in conductivity with temperature (Idris et al., 2007).

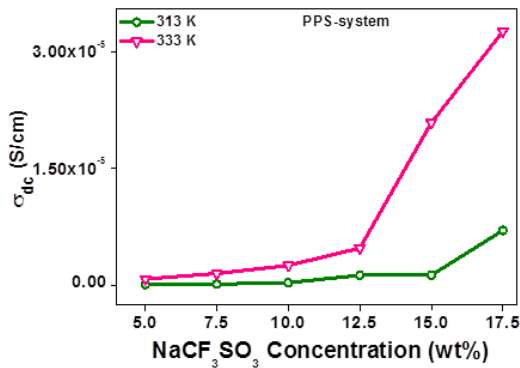


Fig. 5.7 Conductivity as a function of salt concentration.

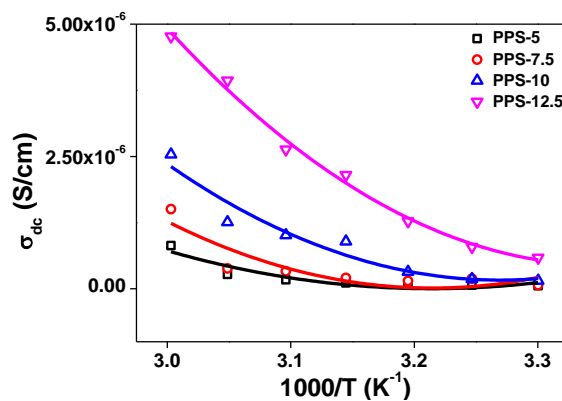


Fig. 5.8 Temperature response of conductivity of PPS samples.

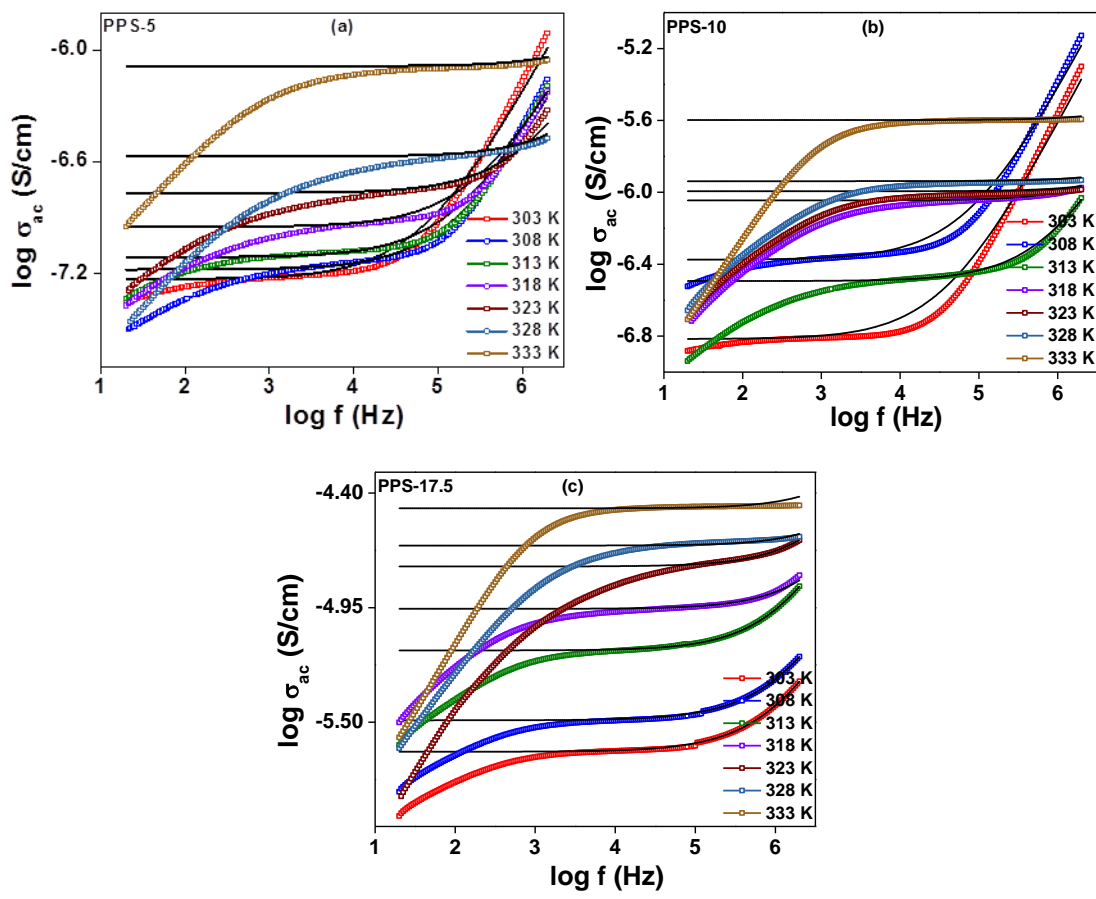
Frequency dependent conductivity for various concentrations of NaCF_3SO_3 is plotted in Figs. 5.9(a-c) and Fig. 5.10 shows frequency dependent conductivity for PPS system. Plots with symbols indicate experimental data and plots with line indicate data fitted according to the Jonscher's power law. Three distinct regions are observed in the plots. Low frequency region is observed due to the electrode-electrolyte interface, the mid-frequency region is independent of frequency and is also called the DC region which is observed due to the diffusion of ions. Higher frequency region depicts the cross-over from DC region to AC region and the dominance of AC mechanism over DC (dispersion region).

Dispersive nature of conductivity with frequency can be well interpreted from Jonscher's Universal Power law (Jonscher et al., 1977).

$$\sigma(\omega) = \sigma_0 + A\omega^n \quad (5.4)$$

where $\sigma(\omega)$ is the value of AC conductivity, σ_0 depicts DC conductivity, A is a constant for a particular temperature and n is the power law exponent related to degree of interaction amongst mobile ions and lattice around them (*Jonscher et al., 1977; Pant et al., 2009*).

The power law exponent n explains conduction mechanism occurring in various types of disordered materials. It is well known (*Jonscher et al., 1977*) that a non-zero n in the dispersive region of conductivity is due to the energy stored in the short range collective motion of ions, a higher n implies that large amount of energy is stored in such collective motions. The process of conduction occurring in the system can be well understood by various models developed to explain the relationship between n and temperature and/or frequency. Overlapping Large Polaron Tunnelling (OLPT) model (*Long, 1982; Ghosh, 1990*) describes the conduction behaviour of the system when n is dependent on frequency as well as temperature and the value of n decreases from 1, with increase in temperature. Correlated Barrier hopping (CBH) (*Elliot, 1982*) model estimates n to be temperature and frequency dependent where n values increase with increase in frequency and decrease with increase in temperature and it, usually takes the value ≈ 0.8 and is temperature independent. However, the conductivity σ_{AC} is explained to be temperature dependent as per QMT model. A small polaron is created when hopping of charge carrier from one site to another causes an overall decrease in energy of the system by a value ω_p (polaron energy). These small polarons are so localized that their distortion clouds do not overlap and hence the name Non-Overlapping Small Polaron Tunnelling (NSPT) model (*Elliot, 1982*). In this case the activation energy required for successful polaron hopping is independent of intersite separation and the power law exponent n is described to be temperature dependent. **Fig. 5.11** shows temperature dependence of power law exponent for PPS system. It clearly shows that the value of n increases with increase in temperature and the conduction mechanism can be attributed due to Non-Overlapping Small Polaron Tunnelling (NSPT) model. All the samples of PPS system show similar response to impedance analysis as that for PPS-17.5 sample.



Figs. 5.9(a-c) Frequency dependent conductivity for various concentrations of NaCF_3SO_3 .

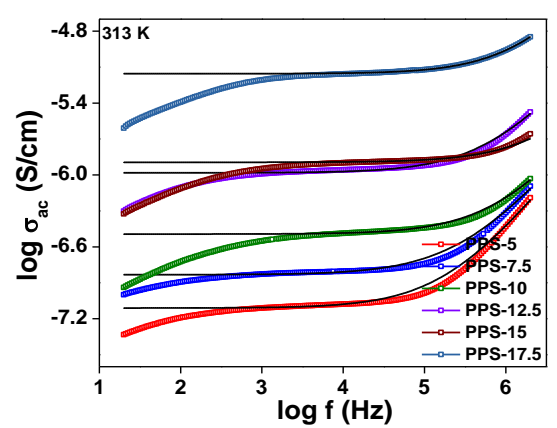


Fig. 5.10 Frequency dependent conductivity for PPS-system.

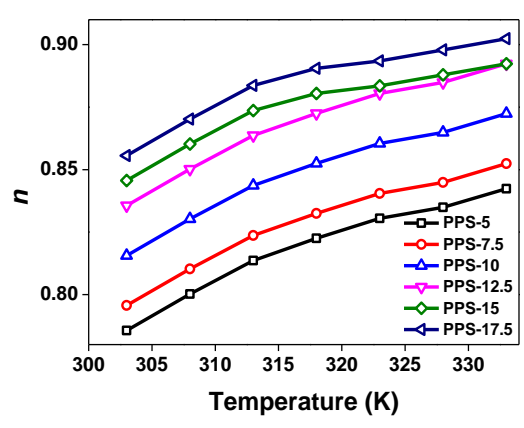


Fig. 5.11 Power law exponent dependence on temperature for PPS-system.

Effect of SHI on ionic conductivity of blend polymer electrolytes

To understand the effect of Swift Heavy Ion (SHI) irradiation on blend electrolytes, all samples of PPS system were subjected to irradiation at four fluences as mentioned above and their response to impedance spectroscopy is discussed below. **Figs. 5.12 (a & b)** show impedance plot of PPS-7.5 and PPS-17.5 samples at different fluences. The

value of R_b decreases upto fluence of 1×10^{12} ions/cm² and then increases at 2×10^{12} ions/cm² fluence. Fig. 5.13 shows impedance plots of PPS-17.5 sample at different temperatures irradiated with fluence of 1×10^{12} ions/cm². R_b decreases with increase in temperature. The equivalent circuit model shown in Fig. 5.4 readily fits the impedance data after irradiation as well. Fig. 5.14 shows fitted impedance plot of PPS-17.5 sample irradiated at various fluences.

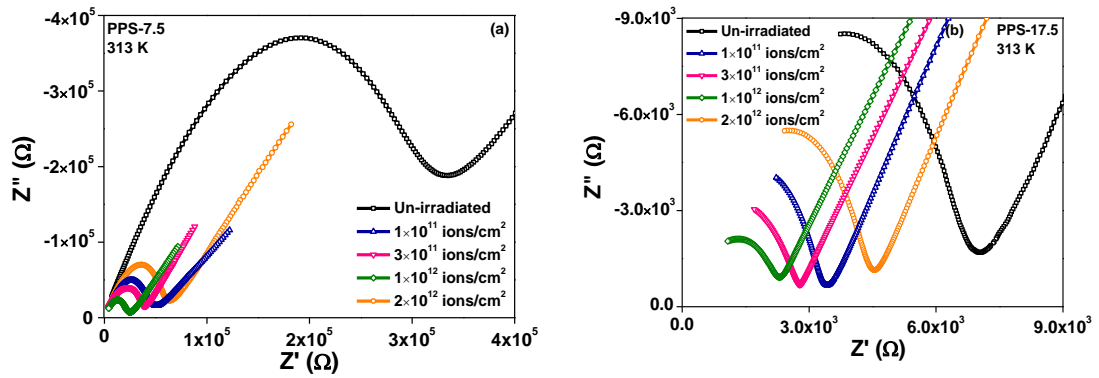


Fig. 5.12 Impedance plots of irradiated (a) PPS-7.5 and (b) PPS-17.5 samples.

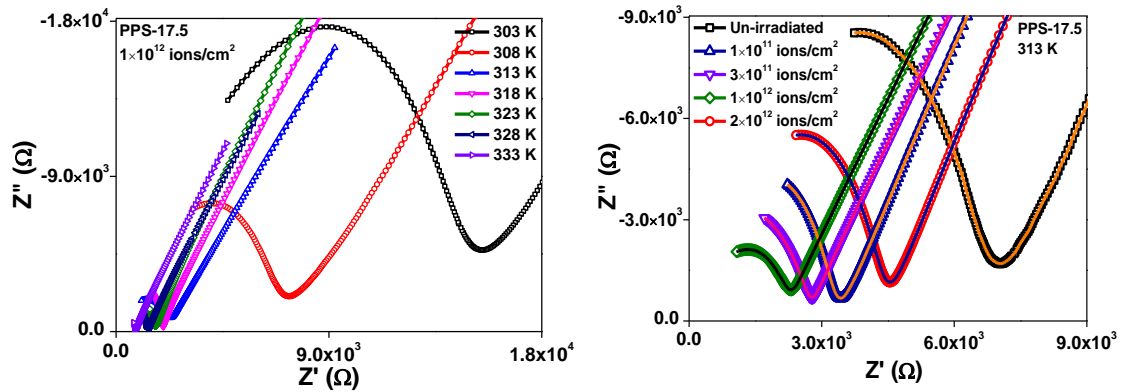


Fig. 5.13 Impedance plots of PPS-17.5 sample at different temperatures irradiated with 1×10^{12} ions/cm² fluence.

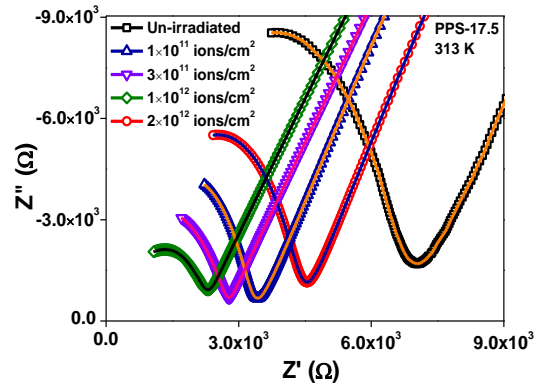


Fig. 5.14 Fitted impedance plot of irradiated PPS-17.5 sample.

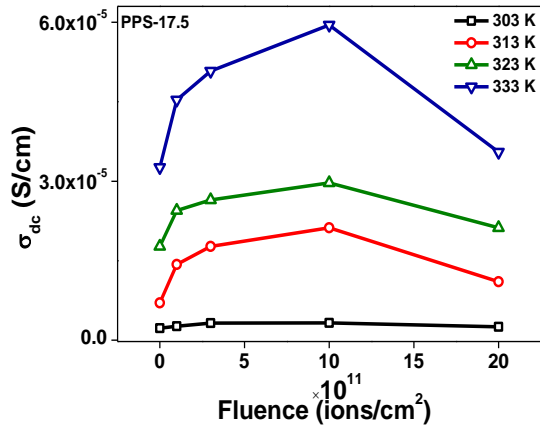


Fig. 5.15 Fluence dependent conductivity for PPS-17.5 sample.

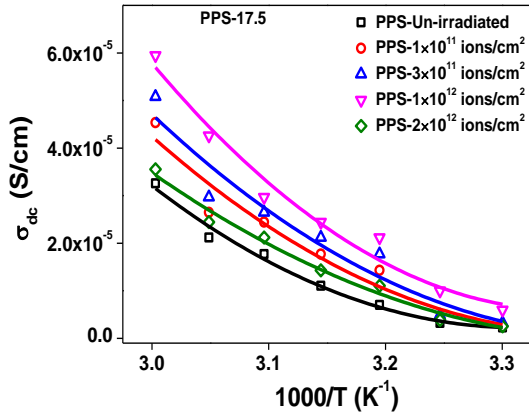


Fig. 5.16 Temperature dependent conductivity for irradiated PPS-17.5 sample.

Fig. 5.15 shows fluence dependence of ionic conductivity for PPS-17.5. Conductivity increases with successive dose up to 1×10^{12} ions/cm² and decreases at 2×10^{12} ions/cm² fluence. Maximum conductivity at room temperature is recorded to be 3.25×10^{-6} Scm⁻¹. The SHI impact at lower fluences is predominated by chain-scissioning process which produces a large number of broken chain segments. Translational motion of these chain segments is the primary reason of increase in ionic conductivity at lower fluences (*Ismayil et al., 2015*). At higher fluence (in our case 2×10^{12} ions/cm²), large number of broken segments cross-link into an ordered matrix. Activation energy required for cross-linking is provided by the critical fluence (1×10^{12} ions/cm² in the present case) above which re-crystallization of the system takes place and apparently conductivity decreases (*Kumar et al., 2010a*). All other samples of PPS system also show similar nature in conductivity with respect to fluence.

Fig. 5.16 shows temperature dependent conductivity for PPS-17.5 sample at different fluences. It is clear that the irradiated samples also follow VTF behavior according to equation 3. During irradiation, the energy deposited in the polymer causes chain fracturing resulting in production of radicals which eventually decay or cross-link with neighbouring radicals. At low fluence, chain scission predominates because of skew radicals present on different chains, which cannot cross-link due to their wide separation. On the other hand, as fluence increases radical concentration increases resulting in formation of closely spaced radicals along the ion track. As a result, coercive interaction among these radical pairs increases, which ultimately allows the

adjacent polymer chains to cross-link (Kumar et al., 2010b). Hema et al. (2017) reported VTF nature of PVA-PVDF nano-composite polymer electrolyte system irradiated with γ -rays, Kumar et al. (2006) reported VTF behavior of Li^{3+} - ion irradiated polymer electrolyte system and Saikia et al. (2006) noted VTF response of swift heavy ion irradiation effects on P(VDF–HFP) based gel polymer electrolytes. All other un-irradiated and irradiated samples of PPS system also follow VTF relation for temperature dependence of conductivity at all the fluences.

Fig. 5.17 shows frequency dependent conductivity of PPS-17.5 sample at various fluences and Fig. 5.18 shows frequency dependent conductivity of PPS-17.5 sample at different temperatures irradiated at fluence of 1×10^{12} ions/cm². For irradiated sample also, three distinct regions are observed. However, the third region becomes insignificant at critical fluence (Fig. 5.17) and at higher temperatures (Fig. 5.18) also. The plots are fitted according to Jonscher's Universal Power law as per equation 4. Fig. 5.19 shows power law exponent n dependence on temperature for PPS-17.5 sample at various fluences. We can see that the values of n increase with increase in temperature and hence NSPT model can be employed to understand conduction mechanism.

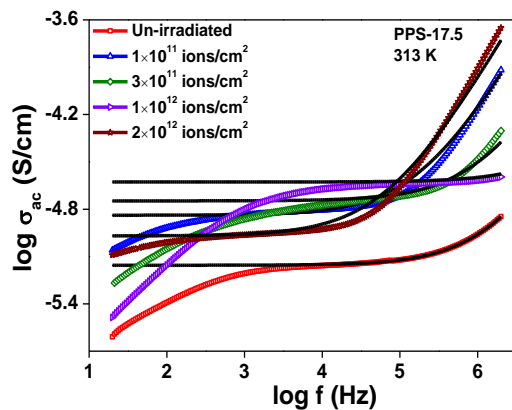


Fig. 5.17 Frequency dependent conductivity for irradiated PPS-17.5 samples.

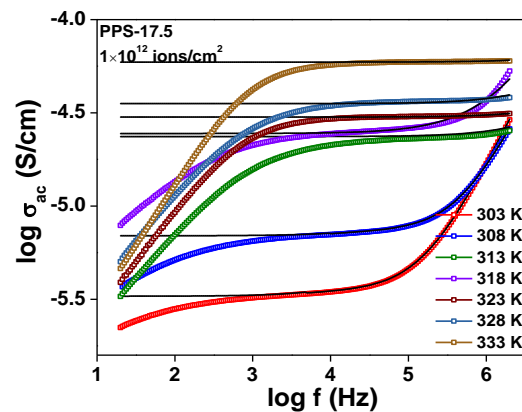


Fig. 5.18 Frequency dependent conductivity of PPS-17.5 sample at different temperatures irradiated with 1×10^{12} ions/cm² fluence.

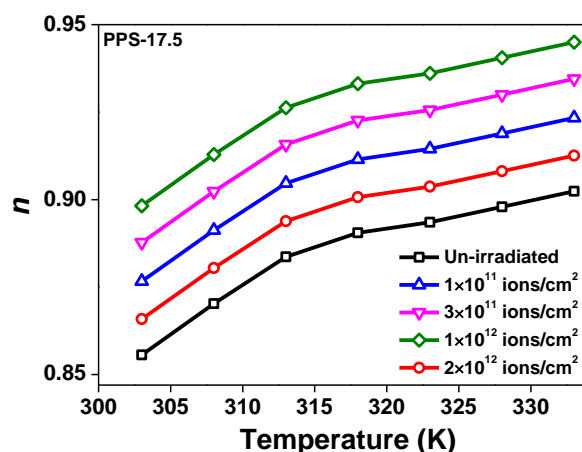


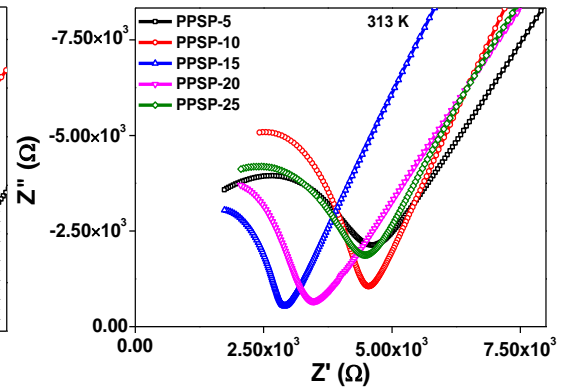
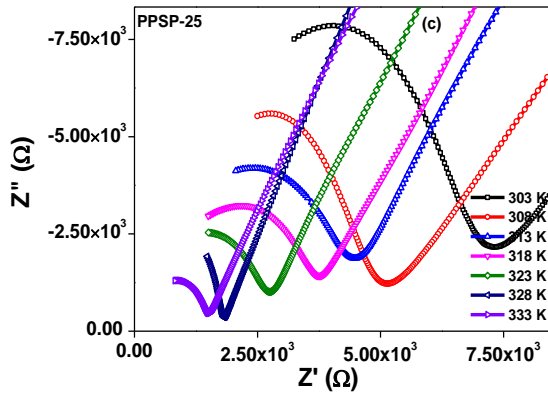
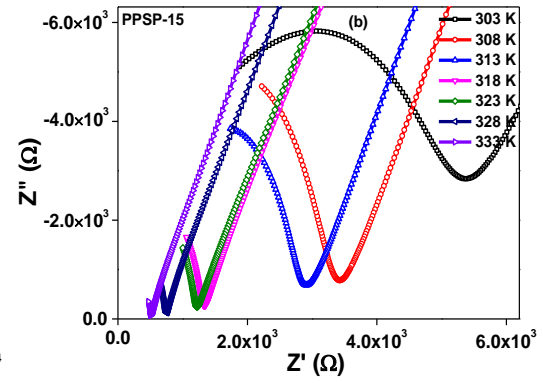
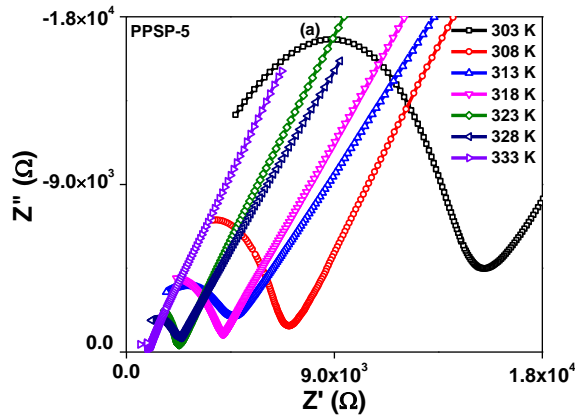
Fig. 5.19 Power law exponent dependence on temperature for irradiated PPS-17.5 sample.

We have observed that the irradiated samples follow the same conduction mechanism which their un-irradiated counterparts do. Although the increase is not very remarkable, irradiation by SHI has definitely led to an increase in ionic conductivity of the BPE system. Also, at higher dose of irradiation, a decrease in ionic conductivity is observed. All other irradiated samples of PPS system show a similar behavior as that for PPS-17.5 sample.

Effect of EC+PC on ionic conductivity

Plasticizers have been widely used as additives (Arunkumar et al., 2017; Das and Ghosh., 2015; Vignarooban et al., 2014; Mathew et al., 2014) to enhance the electrochemical properties of the electrolyte systems. In the present case, we chose PPS-12.5 sample and complexed it with different concentrations of plasticizers to form PPSP system and its response to impedance spectroscopy is discussed below.

Impedance plots for various concentrations of PPSP system are presented in Figs. 5.20(a-c). The impedance plots for all PPSP samples show a semi-circular arc. The bulk resistance R_b is measured from the X-axis intercept of the plot. Values of R_b decrease with increase in temperature for all the PPSP samples. Fig. 5.21 shows the impedance plot of PPSP system at different (EC+PC) concentrations. Values of R_b decrease with increase in EC+PC concentration upto 15 wt% and then increases for 20 wt% and 25 wt% amounts. Fitted impedance plots of PPSP system is shown in Fig. 5.22(a) and Fig. 5.22(b) shows fitted impedance plot for PPSP-15 sample at various temperatures. The circuit used for fitting PPSP samples is shown in the inset of Fig. 5.22(a).



Figs. 5.20(a-c) Impedance plots for various concentrations of EC+PC in PPSP-system recorded at different temperatures.

Fig. 5.21 Impedance plot of PPSP system at different EC+PC concentrations.

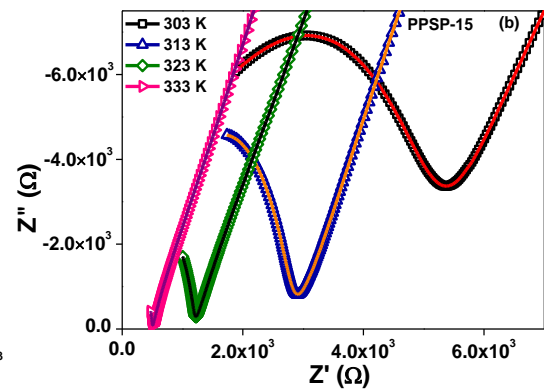
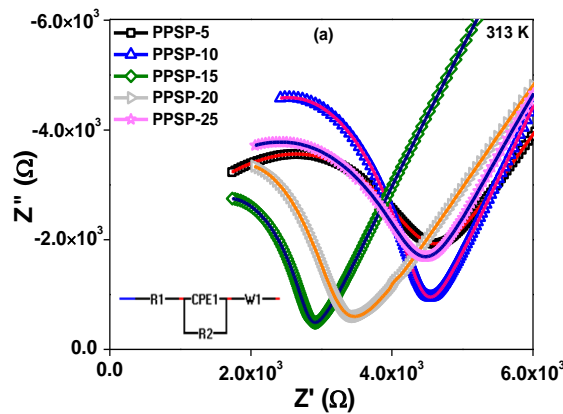


Fig. 5.22 (a) Fitted impedance plot of PPSP-system at 313 K and

(b) Fitted impedance plot of PPSP-15 sample at various temperatures.

Using R_b values, conductivity is calculated as per equation 2. **Fig. 5.23** shows conductivity of PPSP system with (EC+PC) concentration. Values of conductivity increase with increase in (EC+PC) content from 5 wt% - 15 wt% and the slightly decrease for 20 wt% and 25 wt%. Room temperature conductivity value for PPSP-15

sample is recorded to be $9.26 \times 10^{-6} \text{ Scm}^{-1}$. Addition of plasticizer in the blend electrolyte system increases flexibility, ion density, ion mobility and amorphous nature of polymer chain segments (Arunkumar, R et al., 2017) which ultimately lead to an increase in ionic conductivity of the system. However, when the amount of (EC+PC) is very large, e.g. 20 wt% and 25 wt%, the excess plasticizer molecules could start interacting with the polymer blend resulting in decreased ion-polymer blend interactions. Due to this, large number of freely available ions would recombine to form ion-pairs, triplets or ion-aggregates (Song et al., 2017) which inhibits the ion motion and hence the conductivity decreases.

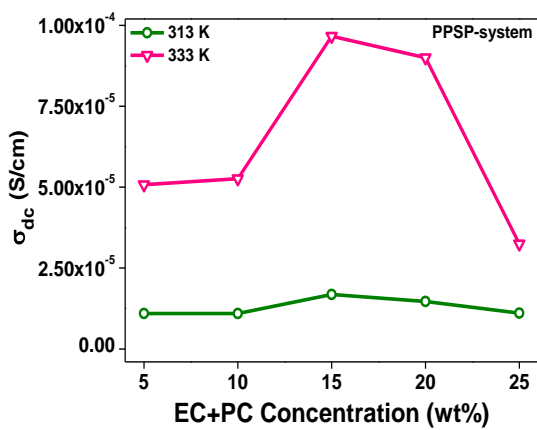


Fig. 5.23 Conductivity as a function of EC+PC concentration.

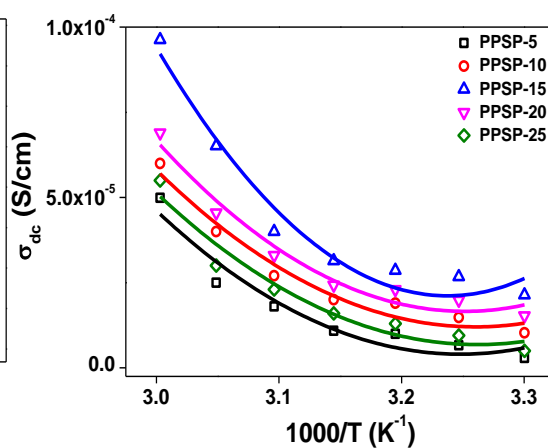
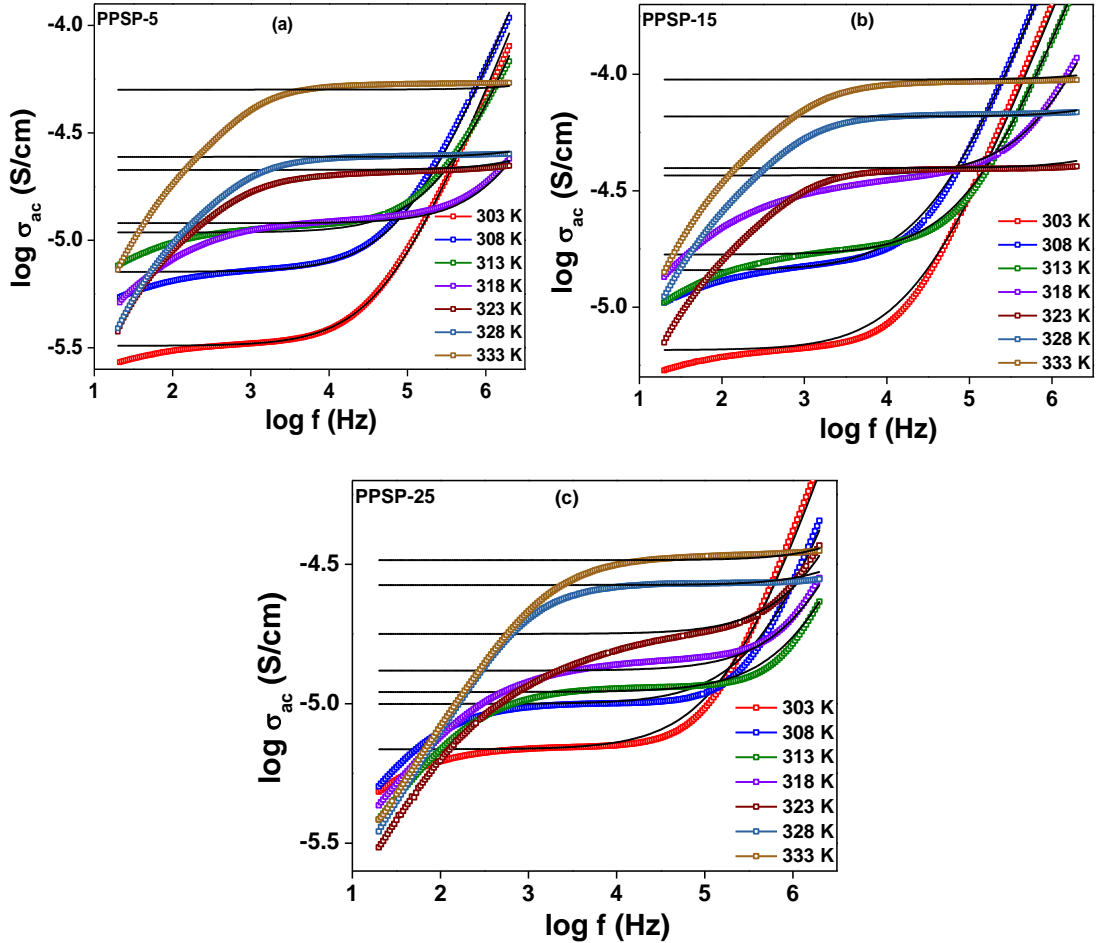


Fig. 5.24 Temperature response of conductivity of PPSP samples.

Fig. 5.24 shows temperature dependent conductivity isotherm for PPSP system. The plasticized blend electrolytes show VTF nature as given by equation 3. Distinguished fits of the conductivity data to the VTF relation over entire temperature range suggests that Na⁺-ion motion is coupled with segmental motion of the polymer chains (Das and Ghosh., 2015). Kumar and Munichandraiah (2000) observed VTF behaviour in PEO-MgTr system plasticized with EC, PC and combination of EC/PC, Das and Ghosh (2015) reported VTF behaviour in PEO-LiClO₄ electrolytes incorporated with PEG, EC, PC and DMC plasticizers. And Pitawala et al. (2007) observed VTF obedience in EC incorporated PEO₉-LiTf-Al₂O₃ system.



Figs. 5.25(a-c) Frequency dependent conductivity for various concentrations of EC+PC.

Frequency dependence of conductivity for plasticized blend electrolyte samples of PPSP system is plotted in **Figs. 5.25(a-c)**. Non-linear relationship of σ vs frequency shows three definite regions. (i) low frequency region displaying electrode polarization effects, (ii) mid frequency dc plateau region corresponding to dc conductivity values and (iii) high frequency region depicting cross-over from DC to AC regime. **Fig. 5.26** shows frequency response of conductivity of PPSP system. Jonscher's power law (equation 4) can readily explain the frequency dependence of conductivity in all above cases of PPSP system. **Fig. 5.27** shows n versus temperature plot of PPSP system. Values of n decrease with increase in temperature and Correlated Barrier Hopping (CBH) model can explain the conduction mechanism in PPSP system. All samples of PPSP system show similar characteristics as that of PPSP-15 sample.

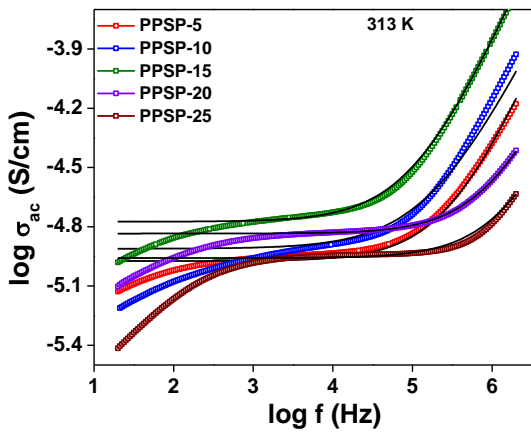


Fig. 5.26 Frequency dependent conductivity for PPSP-system.

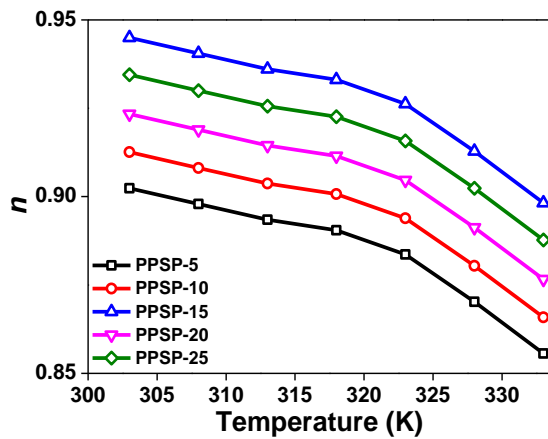


Fig. 5.27 Power law exponent dependence on temperature for PPSP-system.

Addition of plasticizers in BPE samples has led to an increase in ionic conductivity of the system. To further our investigations, all samples of PPSP system were also irradiated at four fluences and below we discuss their response to impedance analysis.

Effect of SHI on ionic conductivity of plasticized blend polymer electrolytes

Figs. 5.28 (a and b) show impedance plots for PPSP-5 and PPSP-15 samples various fluences. The characteristic semicircular arcs are observed for the irradiated samples as well. Values of R_b decrease with increase in fluence up to 1×10^{12} ions/cm² and then increase for fluence of 2×10^{12} ions/cm². Fig. 5.29 shows impedance plot of PPSP-15 sample at different temperatures irradiated at fluence of 1×10^{12} ions/cm². After irradiation also, the values of R_b decrease monotonically with increase in temperature. Equivalent circuit model which fits the un-irradiated samples easily fits irradiated samples as well and the fitted impedance plot for PPSP-15 sample at various fluences is shown in Fig. 5.30.

Fig. 5.31 shows conductivity as a function of fluence for PPSP-15 sample. Conductivity increases with increase in fluence up to 1×10^{12} ions/cm² and then decreases at fluence of 2×10^{12} ions/cm². Room temperature conductivity value for 1×10^{12} ions/cm² fluence is recorded to be 1.78×10^{-5} Scm⁻¹. SHI irradiation creates ample number of broken polymer chains which float through the plasticizer and give higher ionic conductivity at different fluences. At higher fluence i.e., 2×10^{12} ions/cm², cross-linking process dominates in the system inhibiting the conductivity. Ionic conductivity

in all other irradiated samples of PPSP system follows similar behavior with respect to fluence.

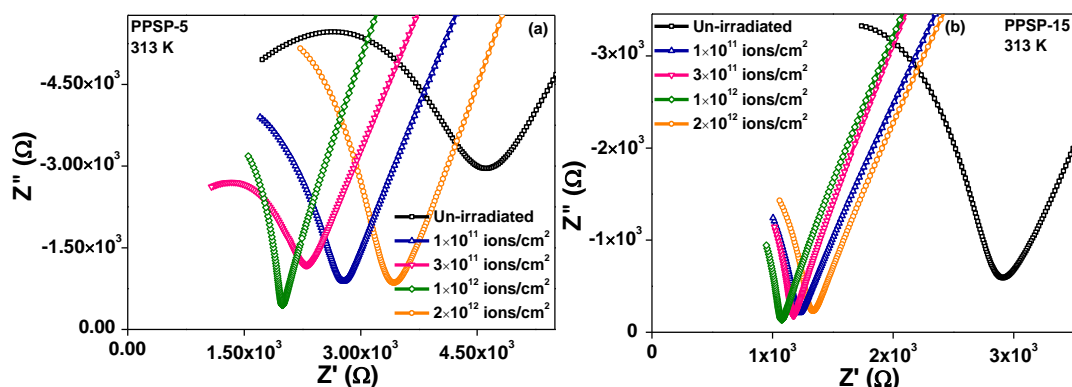


Fig. 5.28 Impedance plots of irradiated (a) PPSP-5 and (b) PPSP-15 samples.

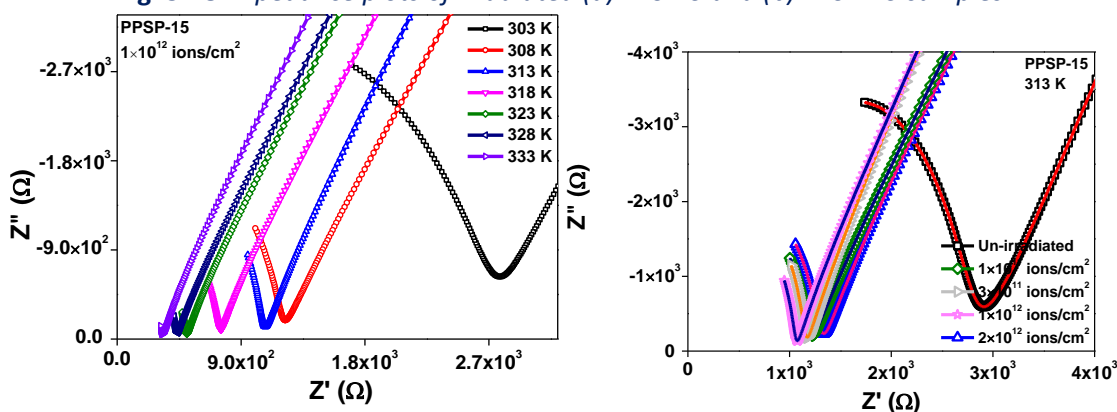


Fig. 5.29 Impedance plots of PPSP-15 sample at different temperatures irradiated with 1×10^{12} ions/cm² fluence.

Fig. 5.30 Fitted impedance plot of irradiated PPSP-15 sample.

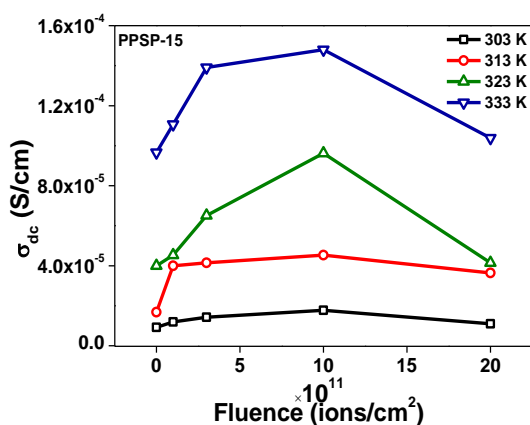


Fig. 5.31 Fluence dependent conductivity for PPSP-15 sample.

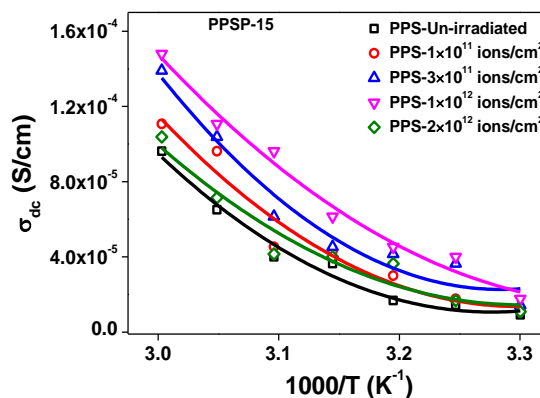


Fig. 5.32 Temperature dependent conductivity for irradiated PPSP-15 sample.

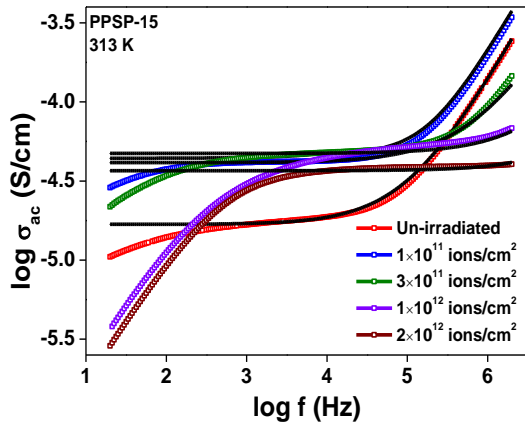


Fig. 5.33 Frequency dependent conductivity for irradiated PPSP-15 samples.

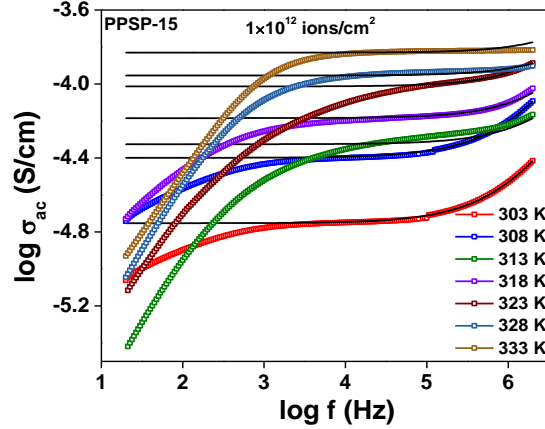


Fig. 5.34 Frequency dependent conductivity of PPSP-15 sample at different temperatures irradiated with 1×10^{12} ions/cm² fluence.

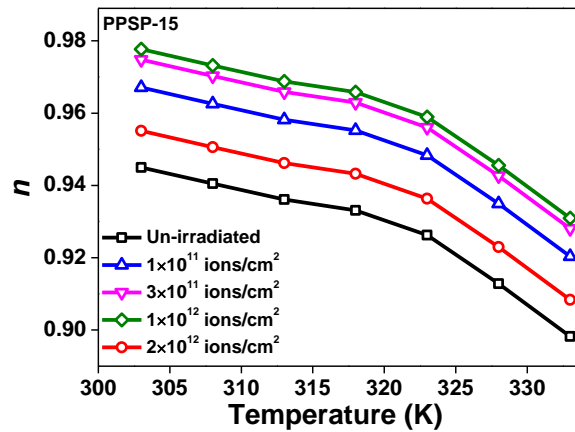


Fig. 5.35 Power law exponent dependence on temperature for irradiated PPSP-15 sample.

Temperature dependent conductivity isotherm for PPSP-15 sample at different fluences are shown in Fig. 5.32. VTF behavior is also observed in the irradiated PPSP samples. Irradiation by ion beam damages the ordered structure of the polymer matrix resulting in broken polymer chains. Plasticizer rich amorphous regions within the polymer electrolyte system facilitate faster segmental motion of these polymer chains at even lower fluence which leads to an increase in ionic conductivity of the system. At higher fluence i.e., 2×10^{12} ions/cm², plasticizer acts as bridge between nearby broken chain segments and promote cross-linkages in the system. The occurrence of cross-links leads to re-establishment of ordered network structure in the polymer matrix which fundamentally decreases ionic conductivity of the system. All samples of PPSP system follow VTF behavior at all fluences. Saikia et al. (2006) observed similar behavior in PC+DEC based gel polymer electrolytes irradiated by Li³⁺-ion, and Diederichsen et al.

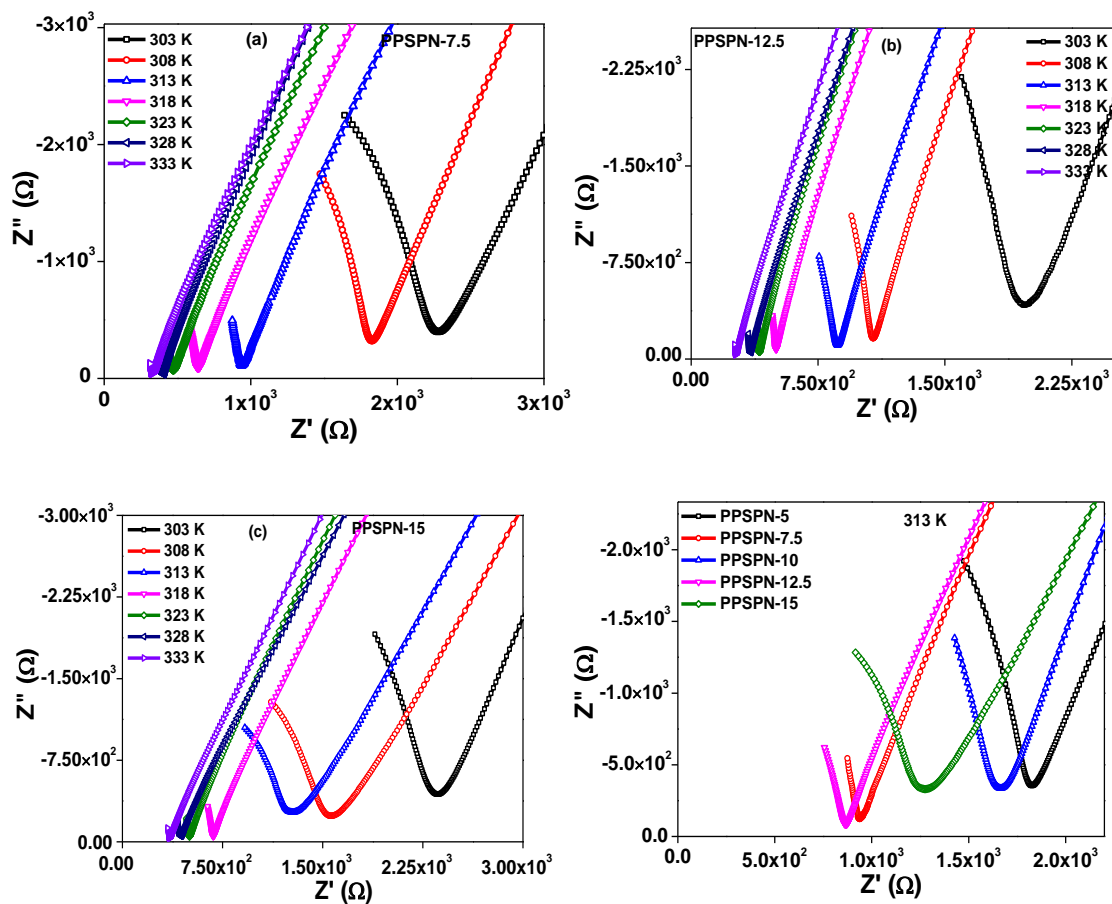
(2017) observed VTF nature in Polysulfone– poly(ethylene glycol) (PSf-co-PEG)-Li⁺ polymer system.

Fig. 5.33 shows frequency response of conductivity of PPSP-15 sample at various fluences and Fig. 5.34 shows frequency response of conductivity of PPSP-15 sample at various temperatures irradiated at critical fluence. Irradiated and un-irradiated samples show similar characteristics and follow Jonscher's Power Law (JPL) behaviour (equation 4). Temperature dependence of power law exponent n for un-irradiated and irradiated PPSP-15 sample have been plotted in Fig. 5.35. It is observed that values of n decrease with increase in temperature which attributes that Correlated Barrier Hopping (CBH) model can be employed to describe this behavior. Thus, irradiation of the plasticized blend electrolyte samples further enhances the ionic conductivity of the system. The increase in ionic conductivity in Irradiated plasticized blend polymer electrolyte samples and un-irradiated samples follow the same conduction mechanism. At higher fluence, the ionic conductivity is observed to decrease. All irradiated samples of PPSP system follow similar variation behavior as that of PPSP-15 sample.

Effect of SiO₂ on ionic conductivity

Another common practice, to enhance electrochemical properties of the electrolytes, is to disperse nano-fillers in the system (Ketabi and Keryn, 2014; Caimi et al., 2018; Choudhary and Sengwa, 2017). In our study, we chose PPSP-20 sample and dispersed different concentrations of SiO₂ and then recorded the impedance response of all the nano-filler dispersed samples. The results are discussed below.

Impedance plots of nano-SiO₂ incorporated plasticized blend electrolyte samples are shown in Figs. 5.36(a-c). Characteristic semi-circular arc is observed in case of each plot. As observed for PPS and PPSP systems, the value of R_b decreases with increase in temperature for all PPSPN samples. Fig. 5.37 shows impedance plot for PPSPN system. The R_b values decrease with increase in SiO₂ content upto 7.5 wt%, again increases at 10 wt%, and 15 wt% while decreases for 12.5 wt%. The fitted impedance plot of PPSPN system, equivalent circuit (Randles cell) is shown in the inset of the Fig. 5.38(a). Fitted impedance plots of PPSPN-12.5 sample at different temperatures is shown in Fig. 5.38(b).



Figs. 5.36(a-c) Impedance plots for various concentrations of SiO_2 in PPSPN system recorded at different temperatures.

Fig. 5.37 Impedance plot of PPSP system at different SiO_2 concentrations.

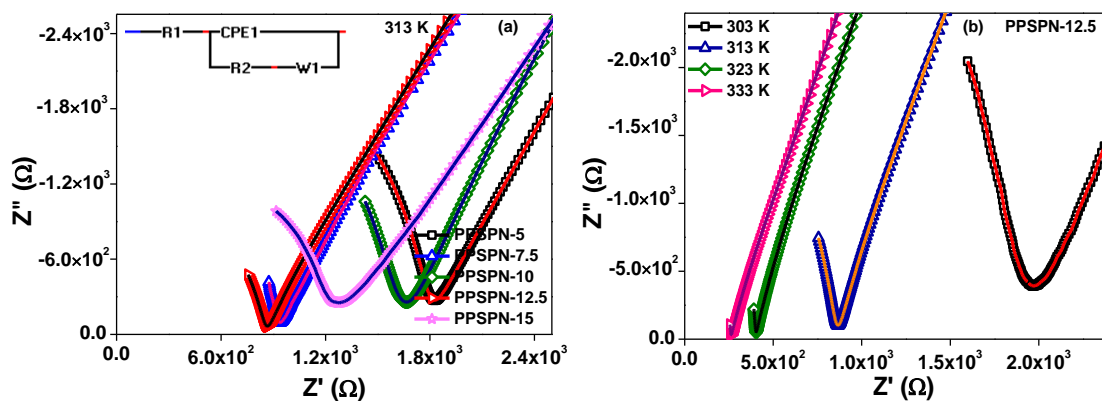


Fig. 5.38 (a) Fitted impedance plot of PPSPN-system at 313 K and **(b)** Fitted impedance plot of PPSPN-12.5 sample at various temperatures.

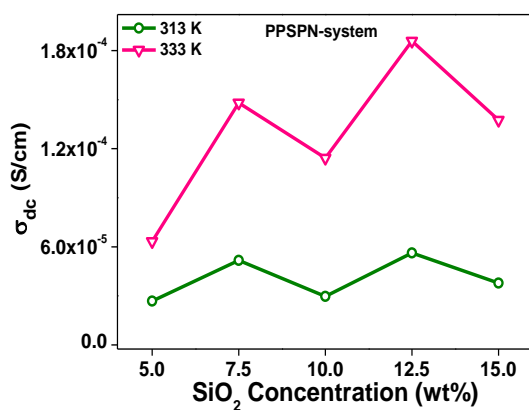


Fig. 5.39 Conductivity as a function of SiO₂ concentration.

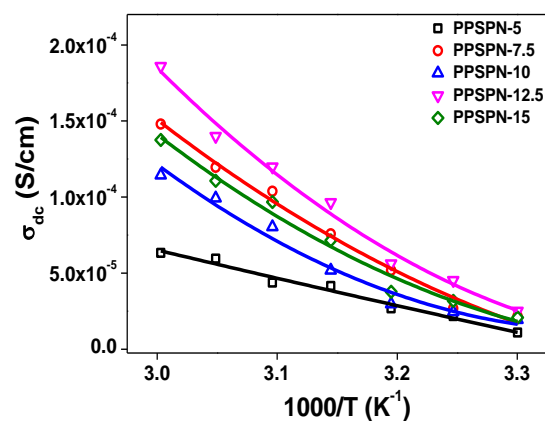
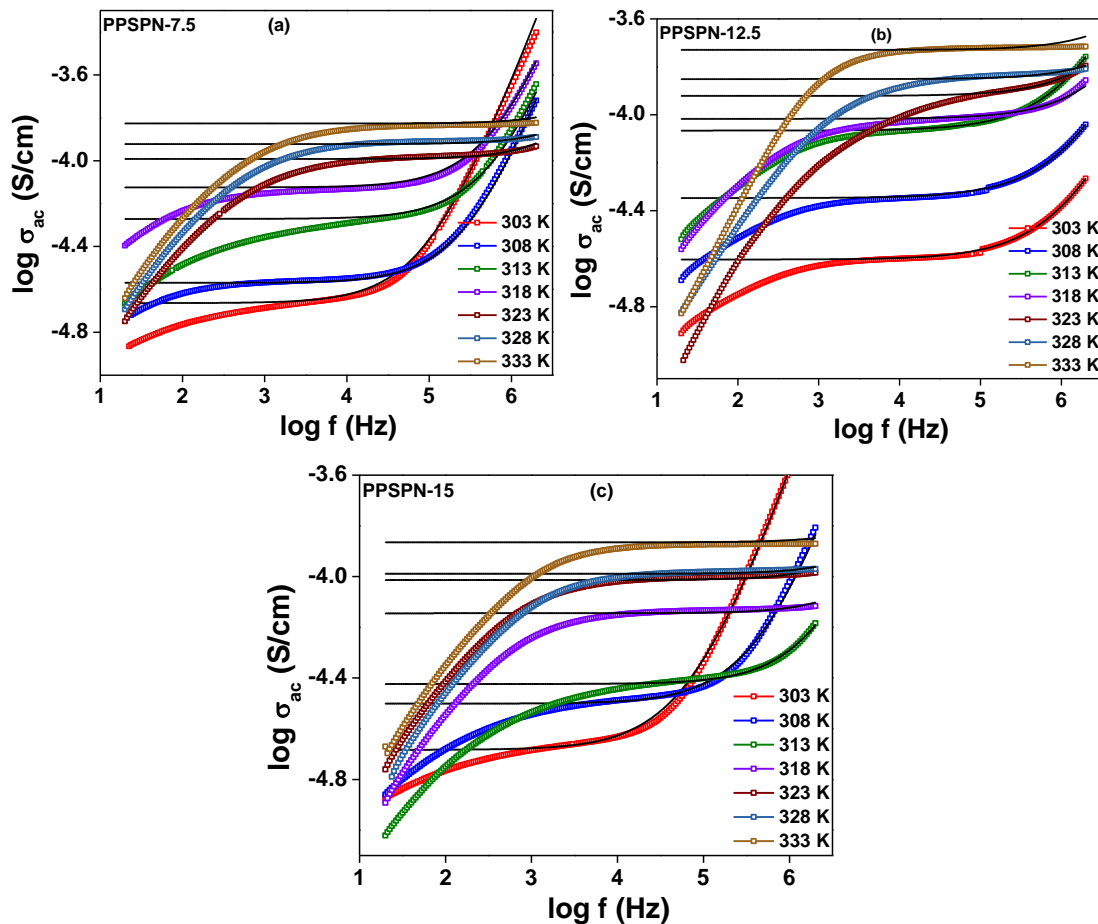


Fig. 5.40 Temperature response of conductivity of PPSPN samples.

Conductivity as a function of SiO₂ content is displayed in Fig. 5.39 which shows, ionic conductivity increases from PPSPN-5 to 7.5 samples, decreases slightly for PPSPN-10 sample, increases to maximum for PPSPN-12.5 sample and decreases slightly again for PPSPN-15 sample. Room temperature ionic conductivity value for PPSPN-12.5 sample is recorded as $2.51 \times 10^{-5} \text{ Scm}^{-1}$. There are two conductivity percolations observed in the figure, one at 7.5 wt% and the other at 12.5 wt% SiO₂. Addition of nano-filler in the system promotes faster ion dissociation due to increase in pathways and Lewis acid-base interaction between polar groups of inorganic filler and the ion species of the electrolyte (Gondaliya et al., 2011). Also *h*-bonding between surface molecules of the filler and ion species weaken ion pair association and lead to an increase in transport number (Money et al., 2012). Initial increase in conductivity with increase in SiO₂ content up to 7.5 wt% is attributed to the Lewis acid-base interaction between polar groups of inorganic SiO₂ and the ion species in the electrolyte and a decrease in this interaction may be the reason for decrease in conductivity at 10 wt%. As the concentration of the filler increases, the conductivity reaches maxima at 12.5 wt%, and then at 15 wt% SiO₂ due to agglomeration of conducting pathways lead to a decrease in ionic conductivity (Abdullah et al., 2009).

Temperature dependence of conductivity for PPSPN system is plotted in Fig. 5.40. VTF behavior as described by equation (equation 3), is observed in all PPSPN samples. Inert nature of nano-filler makes its particles to stay put between the interstices in the host matrix. This creates large free volume in the system subsequently enhancing the conductivity via increased polymer segmental motion. In case of PPSPN system,

segmental motion of polymer chains is assisted due to combined effect of the plasticizer rich amorphous regions and the free volume created due to incorporation of nano-SiO₂ in the system.



Figs. 5.41(a-c) Frequency dependent conductivity for various concentrations of SiO₂.

Frequency dependence of conductivity at various concentrations of SiO₂ is shown in **Figs. 5.41(a-c)**. Frequency dependent conductivity of PPSPN-12.5 sample at various temperatures is shown in **Fig. 5.42**. Three characteristic regions are observed in each of the above cases, and the dispersive nature of plots can be very well explained by Jonscher's Power law (*JPL*) as per equation 4. The dependence of power law exponent n on temperature is shown in **Fig. 5.43**, the values of n increase with increase in temperature and hence can be explained as per Non-overlapping Small Polaron Tunneling (NSPT) model. Thus, nano-filler dispersion has also responded positively, and we have been able to achieve a good room temperature value of conductivity ($2.51 \times 10^{-5} \text{ Scm}^{-1}$). All other samples of PPSPN series show a similar nature as that of PPSPN-12.5 sample.

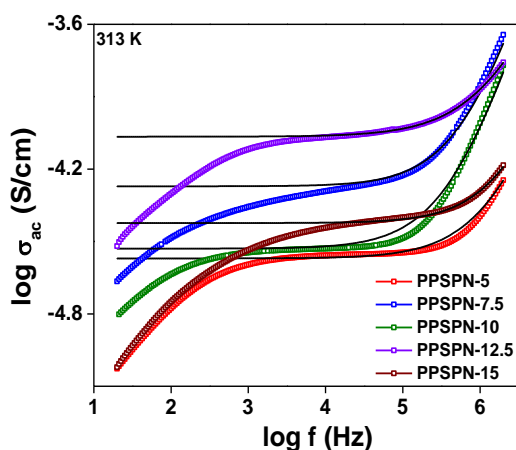


Fig. 5.42 Frequency dependent conductivity for PPSPN-system.

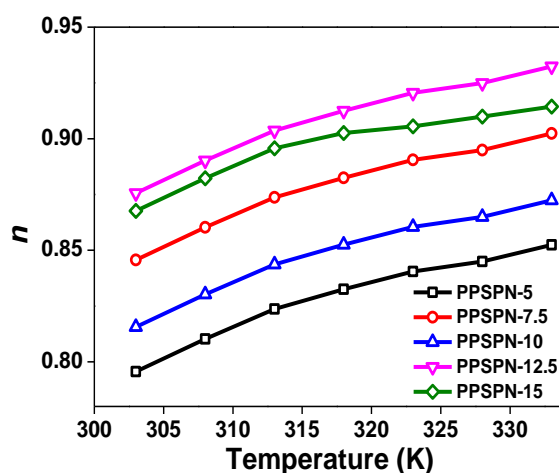


Fig. 5.43 Power law exponent dependence on temperature for PPSPN-system.

Effect of SHI on ionic conductivity of nano-composite plasticized blend polymer electrolytes

For understanding the effect of SHI on nano-dispersed plasticized blend electrolytes, all the samples of PPSPN system were subjected to irradiation at above mentioned four fluences and we discuss the results of the impedance analysis of the samples below.

Figs. 5.44 (a) and (b) show impedance plots of PPSPN-7.5 and PPSPN-12.5 samples irradiated at various fluences. These samples also show the characteristic semi-circular arc. The values of R_b decrease with increase in fluence up to 1×10^{12} ions/cm² and increase at fluence of 2×10^{12} ions/cm². Fig. 5.45 shows impedance plot of PPSPN-12.5 sample at different temperatures irradiated at 1×10^{12} ions/cm² fluence. Randles cell circuit fits the impedance data for PPSPN irradiated samples and Fig. 5.46 shows fitted impedance plots of PPSPN-12.5 sample at various fluences.

Fig. 5.47 shows that the conductivity increases with increase in fluence up to 1×10^{12} ions/cm² and then decreases at 2×10^{12} ions/cm² fluence. Room temperature conductivity value for fluence of 1×10^{12} ions/cm² is recorded as 3.64×10^{-5} Scm⁻¹. The increase in fragmented polymer segments due to SHI irradiation led to an increase in ionic conductivity at lower fluence values. At higher fluence (2×10^{12} ions/cm²), large number of polymer segments cross-link and restore the crystallinity of the system thus decreasing the ionic conductivity. All samples of PPSPN system are in consonance with the change in ionic conductivity with fluence.

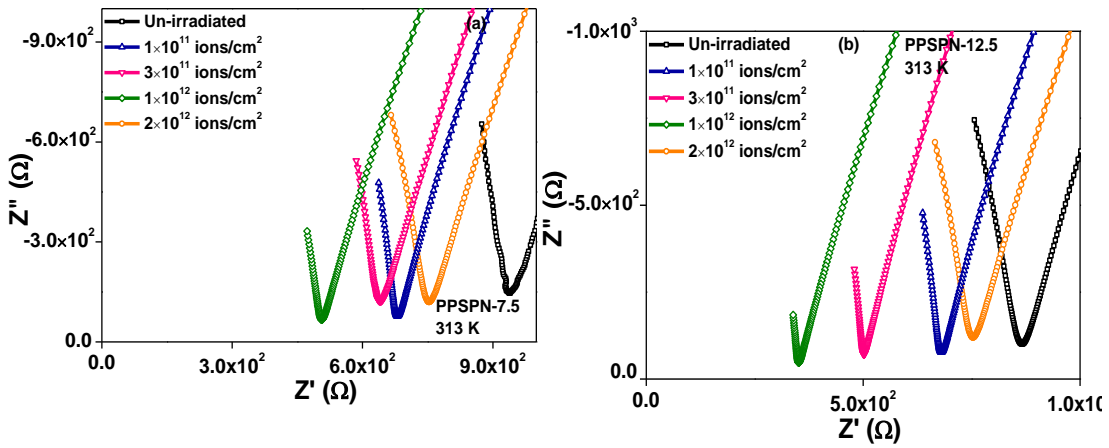


Fig. 5.44 Impedance plots of irradiated (a) PPSPN-7.5 and (b) PPSPN-12.5 samples.

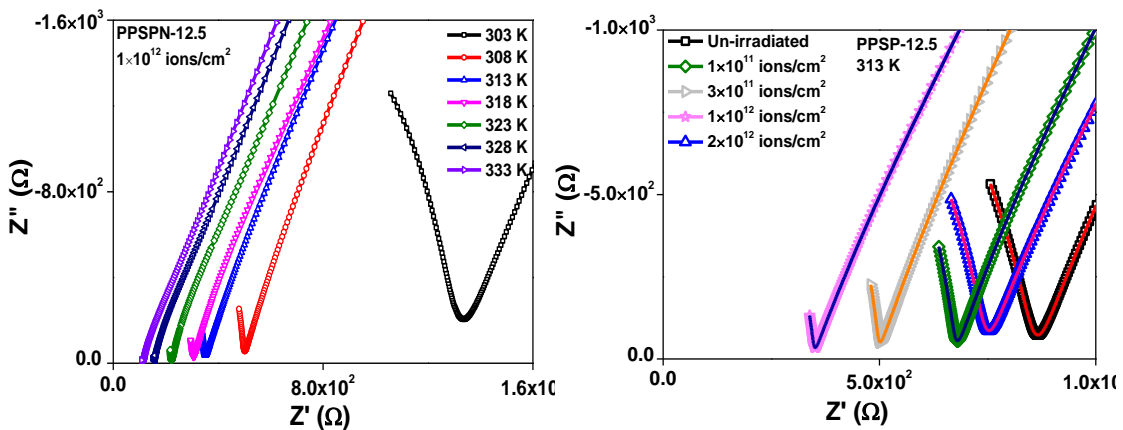


Fig. 5.45 Impedance plots of PPSPN-12.5 sample at different temperatures irradiated with 1×10^{12} ions/cm² fluence.

Fig. 5.46 Fitted impedance plot of irradiated PPSPN-12.5 sample.

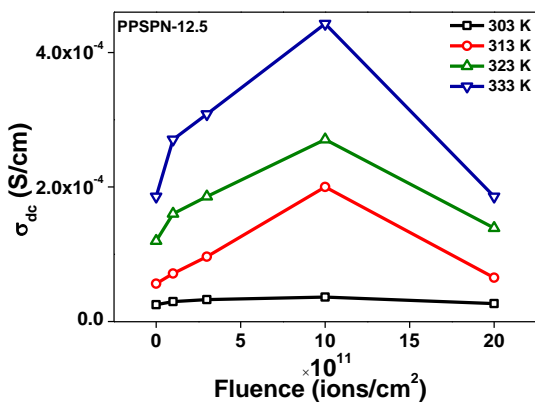


Fig. 5.47 Fluence dependent conductivity for PPSPN-12.5 sample.

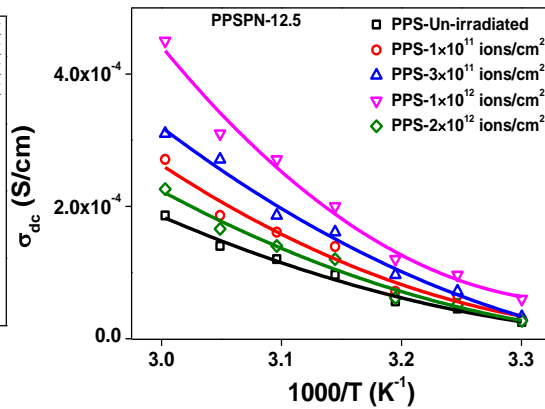


Fig. 5.48 Temperature dependent conductivity of irradiated PPSPN-12.5 sample.

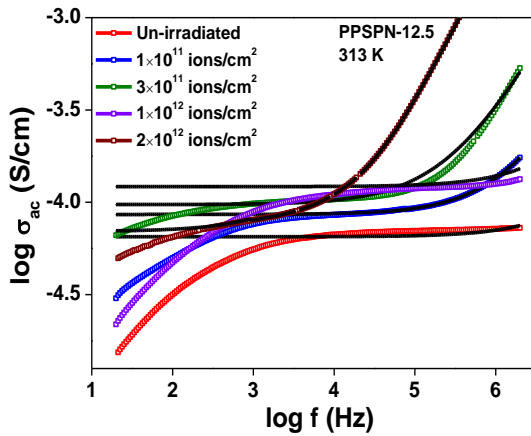


Fig. 5.49 Frequency dependent conductivity for irradiated PPSPN-12.5 sample.

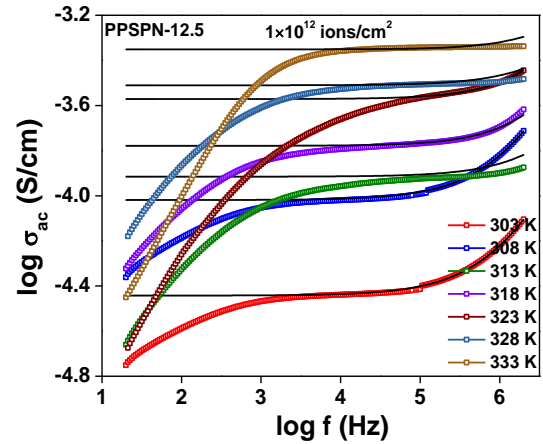


Fig. 5.50 Frequency dependent conductivity of PPSPN-12.5 sample at different temperatures irradiated with 1×10^{12} ions/cm² fluence.

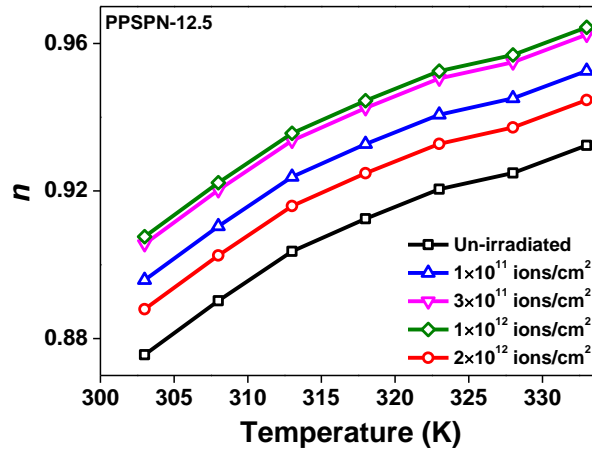


Fig. 5.51 Power law exponent dependence on temperature for irradiated PPSPN-12.5 sample.

Temperature dependent conductivity of PPSPN-12.5 sample irradiated at various fluences is plotted in Fig. 5.48. The irradiated samples also follow VTF behavior according to equation 3. All other irradiated samples of PPSPN system follow VTF behavior in case of temperature dependent conductivity.

Fig. 5.49 shows frequency dependence of ionic conductivity for PPSPN-12.5 sample irradiated at different fluences. Frequency dependent conductivity behavior of PPSPN-12.5 sample at different temperatures for 1×10^{12} ions/cm² fluence is plotted in Fig. 5.50. The frequency dependent behavior follows Jonscher's power law. Power law exponent n versus temperature plot for PPSPN-12.5 sample irradiated at various fluences is given in Fig. 5.51. The values of n increase with increase in temperature it

means the system follows Non-overlapping Polaron Tunneling (NSPT) model. Irradiated samples of the nano-dispersed samples show an increase in the ionic conductivity similar to that of un-irradiated samples. At higher dose of fluence, the polymer films undergo crosslinking process and a decrease in ionic conductivity is expected. Other samples of PPSPN system also show similar nature as that of PPSPN-12.5 sample.

5.2 Dielectric Properties

Electrical behaviour of a system can be probed using dielectric properties and modulus formalism also. Dielectrics are classified as those materials which can store electrical energy. Permittivity of a dielectric material is that property which measures the amount of energy stored in it. Frequency dependent complex dielectric function ϵ^* a material is given as (*Sharma et al., 2013*)

$$\epsilon^*(\omega) = \epsilon'(\omega) - i\epsilon''(\omega) = \frac{1}{i\omega C_0 Z^*} \quad (5.6)$$

Real and imaginary parts of complex impedance Z^* can be used to evaluate real and imaginary parts of the permittivity.

$$\epsilon'(\omega) = \frac{-Z_i}{\omega C_0 (Z_r^2 + Z_i^2)} \quad (5.7)$$

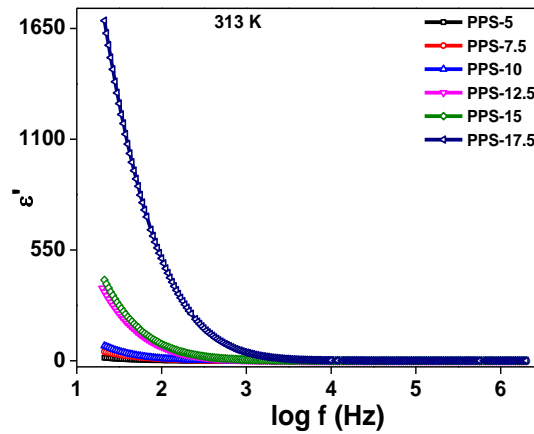
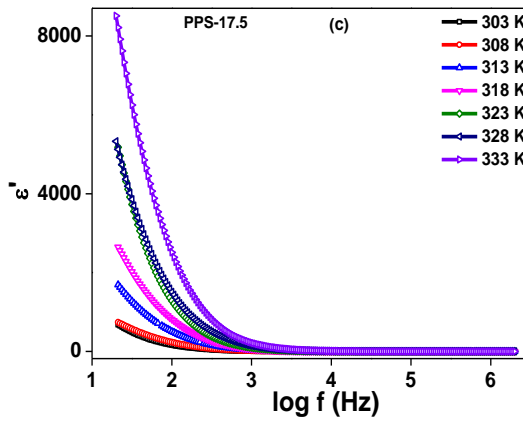
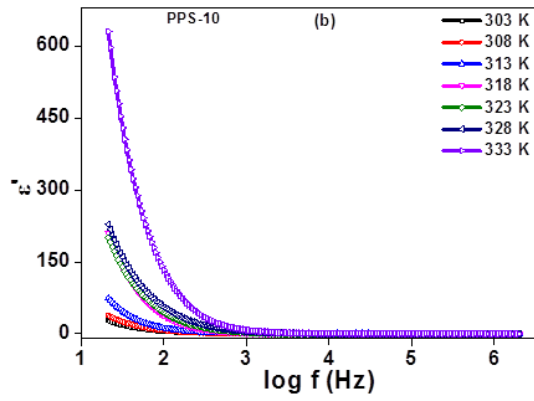
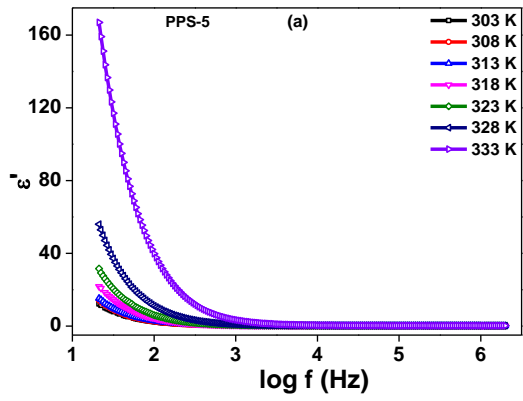
$$\epsilon''(\omega) = \frac{-Z_r}{\omega C_0 (Z_r^2 + Z_i^2)} \quad (5.8)$$

where, C_0 is the capacitance of the material in vacuum, $\omega = 2\pi f$, is the angular frequency and f is the frequency of the applied electric field. Real part of permittivity ϵ' corresponds to ordinary dielectric constant of the material which measures the amount of elastic energy stored in the material during every cycle of applied alternating field and the energy responded back to the field at the end cycle. In this section, we shall discuss about the dielectric response of the three systems of blend electrolytes synthesized by us along with their irradiated counterparts.

Effect of NaCF₃SO₃ on dielectric properties

Figs. 5.52(a-c) shows dielectric response for various concentrations of NaCF₃SO₃. The dielectric decreases with increase in frequency and becomes nearly constant beyond certain frequency. From the figures, it is also clear that the dielectric increases with increase in temperature. Fig. 5.53 shows dielectric constant as a function NaCF₃SO₃,

ϵ_r values increase with increase in salt concentration continuously and show maximum value for PPS-17.5 sample. Higher salt concentration and high temperature induces a greater number of dipoles which follow the field reversal and the values of dispersion frequency shifts towards higher frequency. In case of fast ion conductors, relaxation peaks in ϵ_r are rarely perceptible (*Jonscher, 1978*), so is true in our case. In absence of any relaxation peaks in ϵ_r plots, the values of ϵ_r are used to confirm that the increase in conductivity is occurring primarily due to the increase in number density of the mobile charge carriers (*Ibrahim et al., 2012*). Application of external electric field induces formation of dipoles in the dielectric materials which are polarized in the direction of the field. At lower frequencies, these dipoles are able to align themselves parallel to the field direction and hence the value of dielectric constant is higher. At higher frequencies, change in the electric field is very fast which the dipoles cannot follow and hence their contribution to polarization approaches a small value (*Sharma et al., 2013*). According to *Gupta and Prajapati (2009)*, Correlated Barrier Hopping (CBH) model explains this phenomenon in terms of inter-well and intra-well hopping of the charge carriers. Average distance of inter-well hopping is few nm and that for intra-well hopping is of the order of one lattice spacing. At low frequency, the average relaxation time of the charge carriers is high and hence inter-well hopping mechanism is favoured which leads to increase in dielectric constant. Whereas, at higher frequencies, intra-well hopping is the governing mechanism because the charge carriers have barely enough time to move before which field reversal comes in and hence the dielectric constant decreases (*Biju and Khadar, 2003*). For each of the SPE samples, we have calculated the dispersion frequency and plotted it as a function of NaCF_3SO_3 and temperature in *Fig. 5.54* and *Fig. 5.55* respectively. The dispersion frequency values increase monotonically with increase in salt concentration and temperature, which manifests from the ϵ_r plots.



Figs. 5.52(a-c) Dielectric response for various concentrations of NaCF_3SO_3 .

Fig. 5.53 Dielectric response of PPS-system.

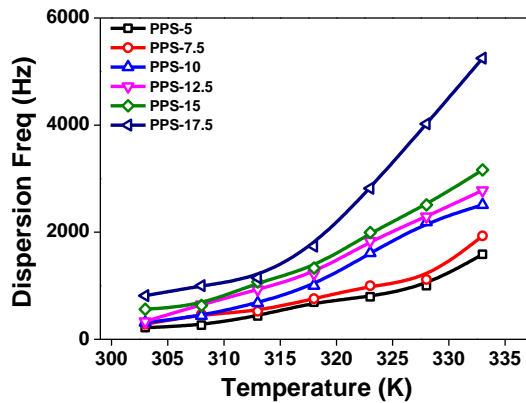
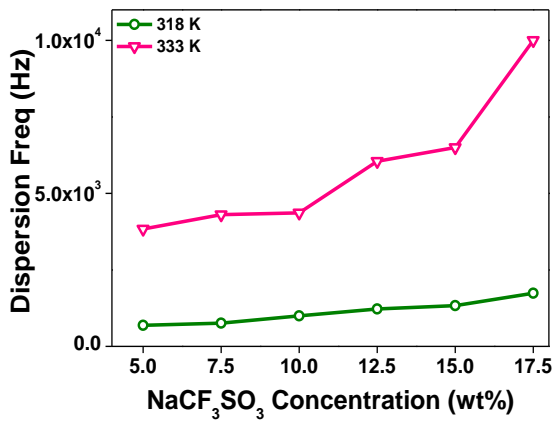
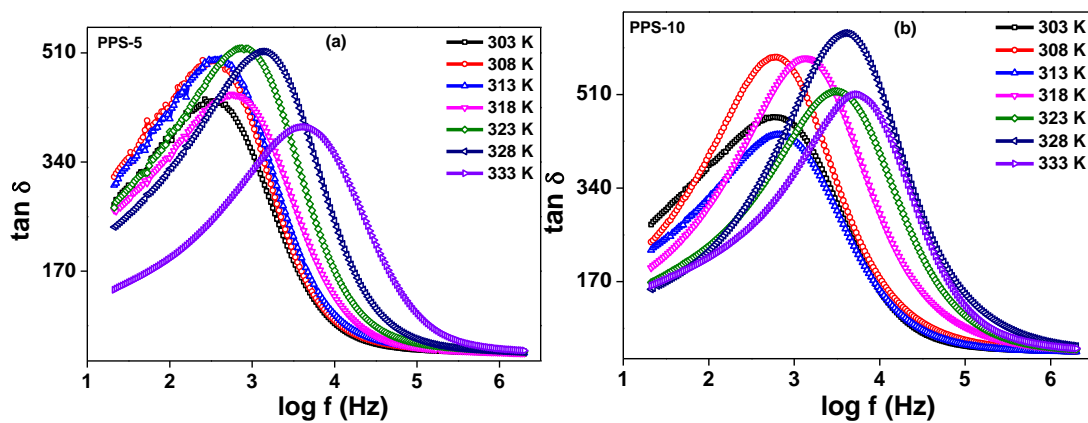


Fig. 5.54 Dispersion frequency as a function of NaCF_3SO_3 concentration.

Fig. 5.55 Dispersion frequency as a function of temperature.

Dielectric loss spectra give the measure of energy loss occurring due to charge transport and electrode polarization effect in the system. **Figs. 5.56(a-c)** show dielectric loss tangent ($\tan \delta$) for various concentrations of NaCF_3SO_3 and the dielectric loss tangent

for PPS system is shown in Fig. 5.57. The $\tan \delta$ values increase with increase in frequency, reach a maximum value and then decrease for higher frequencies. Also, the peak shifts towards higher frequency with increase in temperature and salt concentration. Ibrahim et al. (2012) observed that the peak values increased with increase in temperature, but it is not true for our case. On application of electric field to dielectric material, electrode polarization occurs due to deposition of charges, forming dipoles at the electrodes. These dipoles are forced to oscillate with the frequency same as that of the applied field and this gives rise to a relaxation phenomenon very similar to dipolar relaxation (Coelho, 1983). Occurrence of peak in loss spectra is a manifestation of dipolar relaxation phenomenon. The peak frequencies are plotted as a function of salt concentration and temperature in Fig. 5.58 and Fig. 5.59 respectively. The peak frequency increases with increase in salt concentration and show a maxima for PPS-17.5 sample. With increase in temperature, there is a linear rise in the values of peak frequencies. These figures present a clear picture of the dielectric loss behaviour with addition of NaCF_3SO_3 and increase in the temperature. Increase in amount of NaCF_3SO_3 and temperature, increases the probability of formation of dipoles which contribute to the relaxation process in the system and hence an increase in loss is observed. Generally, in salt-in-polymer type of electrolyte type of systems, there exist optimum amount of salt, beyond which the conductivity and the dielectric properties deteriorate. But this is not true for our case hence we only see linear rise in loss tangent with salt concentration.



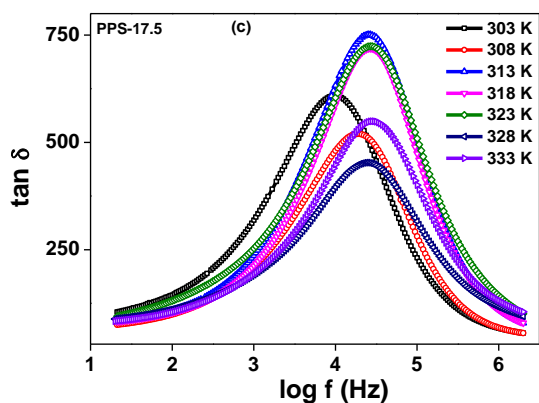


Fig. 5.56(a-c) Dielectric loss for various concentrations of NaCF_3SO_3 .

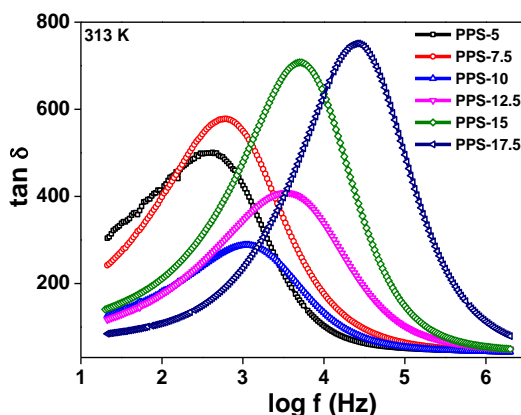


Fig. 5.57 Dielectric loss of PPS-system.

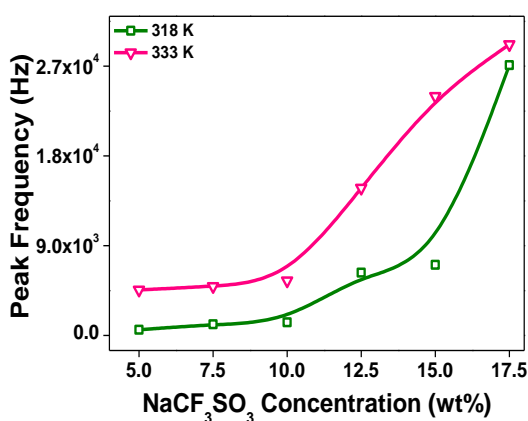


Fig. 5.58 Peak frequency as a function of NaCF_3SO_3 concentration.

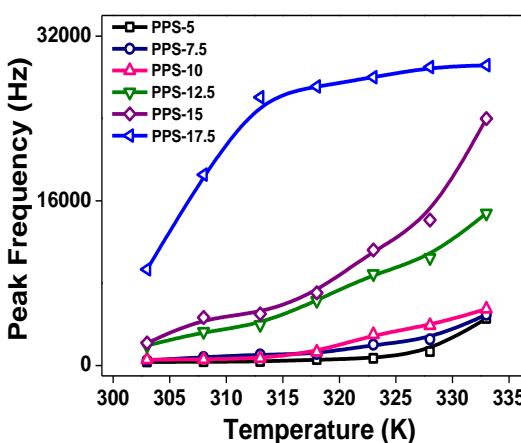


Fig. 5.59 Peak frequency as a function of temperature for PPS-system.

Effect of SHI on dielectric properties of blend polymer electrolytes

Figs. 5.60 (a and b) respectively show dielectric response of PPS-7.5 and PPS-17.5 samples irradiated at various fluences. The dielectric values decrease with increase in frequency and attain a steady value at higher frequency. Also, the value of ϵ_r increases with increase in fluence from 1×10^{11} ions/cm² to 1×10^{12} ions/cm² (critical fluence) and decreases at 2×10^{12} ions/cm² fluence. Fluence response of dispersion frequency for PPS-7.5 and PPS-17.5 samples is plotted in Fig. 5.61 to ascertain the effect of irradiation on the electrolytes. The dispersion frequency values increase up to critical fluence and then decrease at 2×10^{12} ions/cm² fluence. When a polymer material is subjected to irradiation by SHI, the processes of chain scissioning and cross-linking are triggered simultaneously in it. This leads to formation of defects such as bending and breaking of bonds, formation of new polar bonds and production of radicals (Lee, 1999). The fractured segments in polymer matrix act as dipoles which are oriented in

the direction of the applied electric field. The irradiation of polymers increases the orientational polarization due to increase in number of dipoles with fluence (*Kalia et al., 2018*) which leads to increase in dielectric constant. As discussed in conductivity section of the present work, chain scission process dominates at lower fluences and hence more number of segments is available to participate in the orientational polarization process. At higher fluences (in the present case 2×10^{12} ions/cm²) cross-linking process takes over and hence the dielectric constant decreases due to decrease in number of segments effectively participating in the polarization process. *Ismayil et al. (2015)* have observed enhanced dielectric properties after γ -irradiation in PVA-NaBr composites. *Bobby et al. (2016)* have discussed the modifications induced by swift heavy C⁴⁺- ion irradiation on capacitance and dielectric properties of Ni/oxide/n-GaAs schottky diode. Fig. 5.62 shows temperature response of ϵ_r plots for PPS-17.5 sample irradiated with 1×10^{12} ions/cm² fluence. We observed that the ϵ_r values increase with increase in temperature. The dispersion frequency values are observed to follow similar trend as a function of temperature for 1×10^{12} ions/cm² fluence irradiated PPS-17.5 sample in Fig. 5.63. The dielectric loss of PPS-7.5 and PPS-17.5 samples irradiated at various fluences are shown in Fig. 5.64(a) and (b) respectively. The loss values increase with fluence from 1×10^{11} ions/cm² to 1×10^{12} ions/cm² (critical fluence) but decrease at 2×10^{12} ions/cm² fluence. Fluence response of peak frequency for PPS-7.5 and PPS-17.5 samples is plotted in Fig. 5.65 to elaborate the effect of irradiation on the electrolytes. The peak frequency values increase up to 1×10^{12} ions/cm² fluence and then decrease at higher fluence.

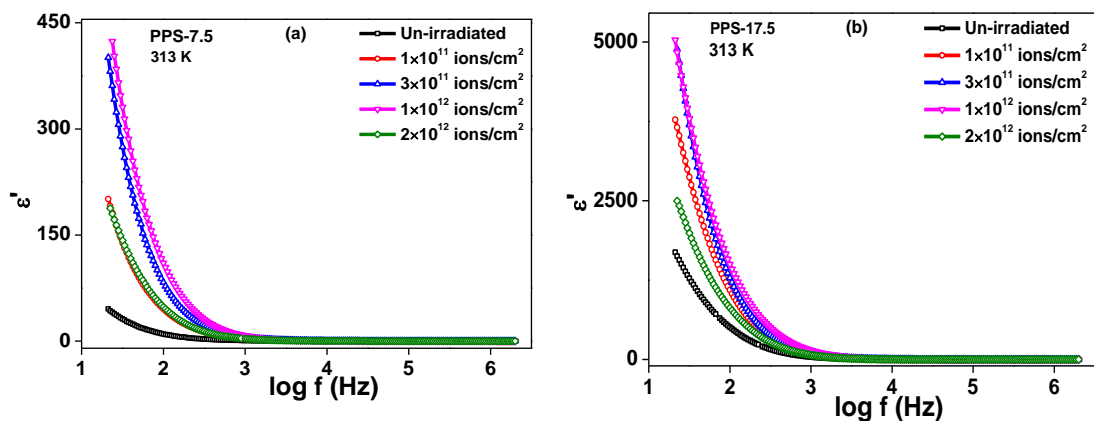


Fig. 5.60 Dielectric response of irradiated (a) PPS-7.5 and (b) PPS-17.5 samples.

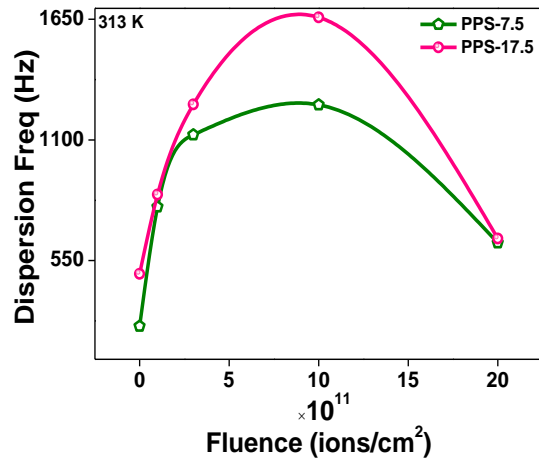


Fig. 5.61 Dispersion frequency as a function of fluence for PPS-7.5 and 17.5 samples.

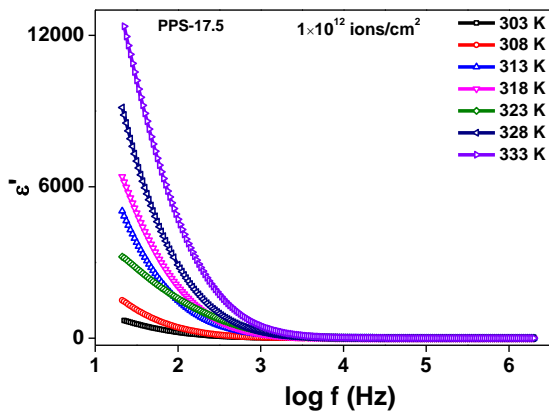


Fig. 5.62 Dielectric response of PPS-17.5 sample irradiated at 1×10^{12} ions/cm² fluence.

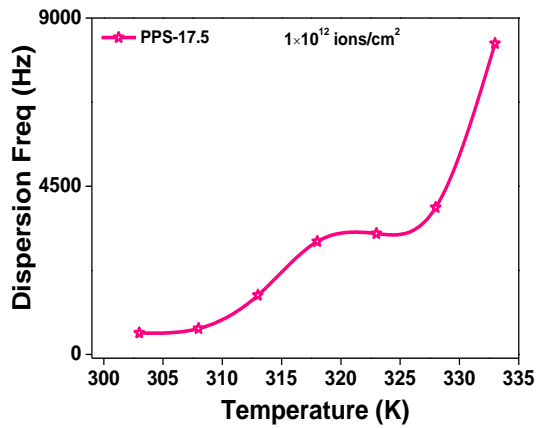


Fig. 5.63 Dispersion frequency of PPS-17.5 sample irradiated at 1×10^{12} ions/cm² fluence.

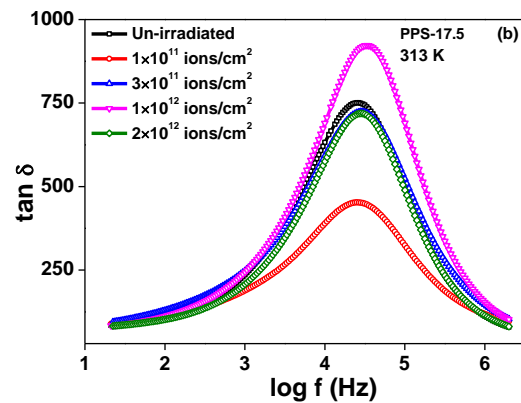
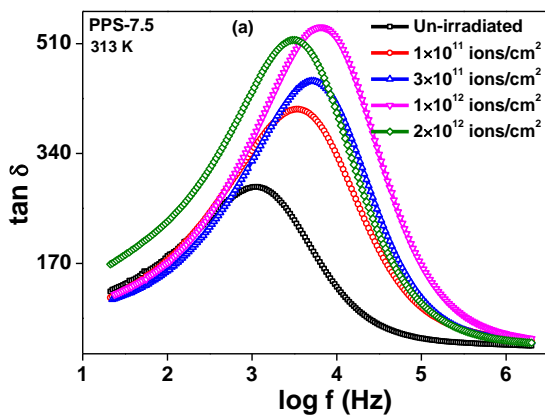


Fig. 5.64 Dielectric loss of irradiated (a) PPS-7.5 and (b) PPS-17.5 sample.

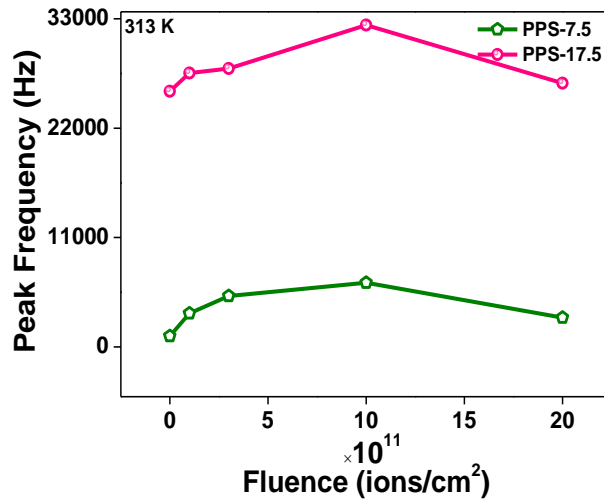


Fig. 5.65 Peak frequency as a function of fluence for PPS-7.5 and 17.5 samples.

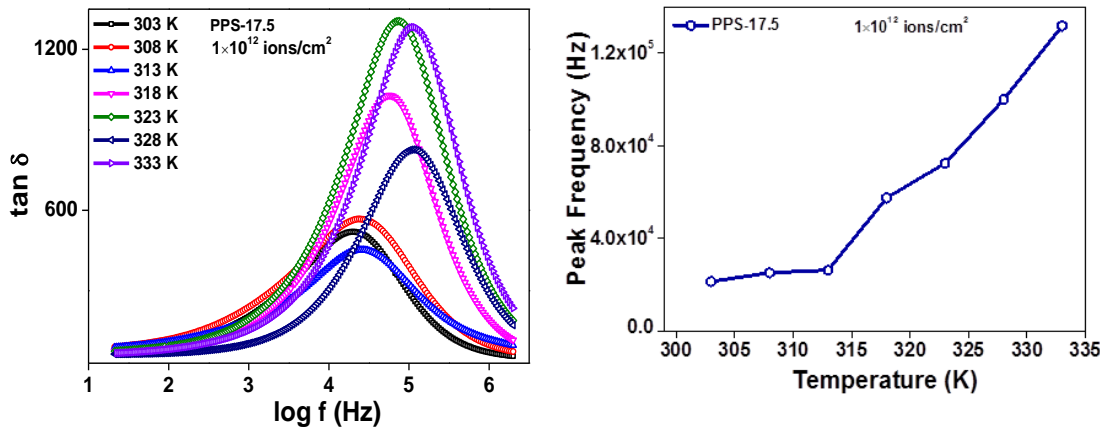


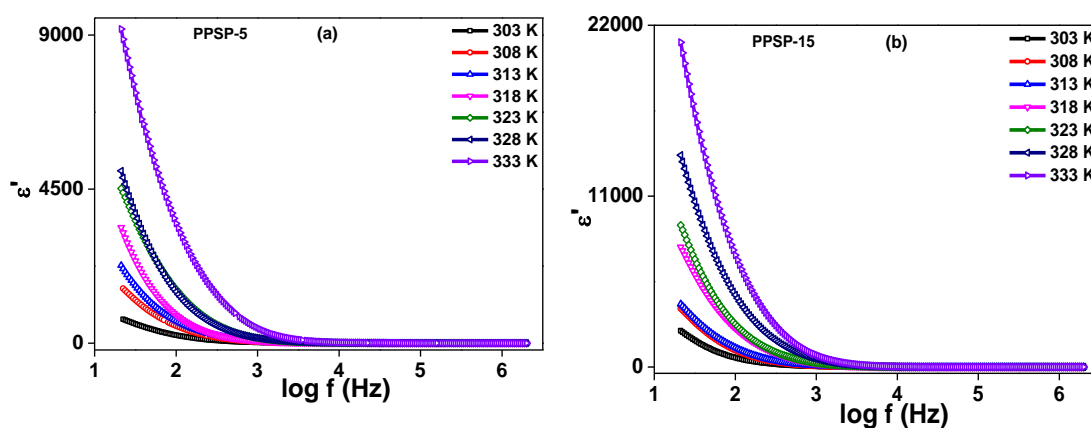
Fig. 5.66 Dielectric loss of PPS-17.5 sample irradiated at 1×10^{12} ions/cm² fluence.

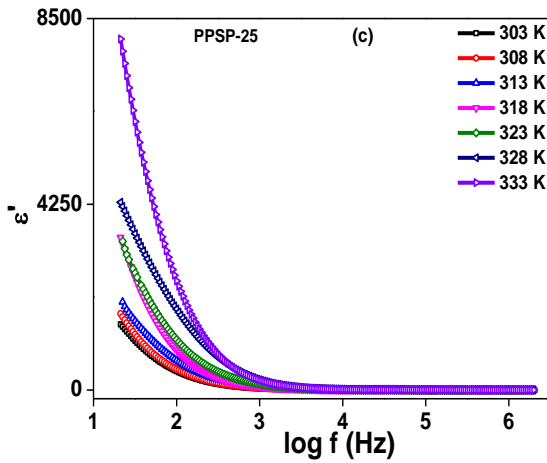
Fig. 5.67 Peak frequency of PPS-17.5 sample irradiated at 1×10^{12} ions/cm² fluence.

Fig. 5.66 shows temperature response of $\tan \delta$ plots for PPS-17.5 sample irradiated with 1×10^{12} ions/cm² fluence. The $\tan \delta$ values increase with increase in temperature and the peak frequency values are observed to follow similar trend as a function of temperature for 1×10^{12} ions/cm² fluence irradiated PPS-17.5 sample given in Fig. 5.67. The linear rise in peak frequency with rise in temperature is due to the fact that the dielectric losses are a combinational consequence of conductivity losses, vibrational losses and dipole losses, the conductivity losses being proportional to σ/ω (where σ is the conductivity and ω is the angular frequency), rise with increase and temperature and fluence (Stevens, 1957).

Effect of EC+PC on dielectric properties

To understand the presence of plasticizer on electrolytic properties in PPS system, we now see how plasticization affects the dielectric properties of BPE samples. Figs. 5.68(a-c) show dielectric response for various concentrations of EC+PC and the dielectric nature of PPSP system is shown in Fig. 5.69. The values of real part of dielectric ϵ_r increase with increase in EC+PC content up to 15 wt%, (ϵ_r shows maximum value) and then decrease afterwards for 20 and 25 wt%. The graphs exhibit common features of low frequency dispersion and retaining a steady state value (low) at high frequency. Addition of plasticizer leads to an increase in localization of ionic species which is the reason for such behaviour (Pradhan *et al.*, 2008). The dispersion frequency values for PPSP samples as a function of EC+PC concentration is plotted in Fig. 5.70. As expected, the dispersion frequency values follow the same trend as that of ϵ_r values. Dispersion frequency increases with increase in EC+PC concentration up to PPSP-15 and then decreases for PPSP-20 and PPSP-25 samples. Initial increase in dispersion frequency is due to the fact that on addition of EC+PC, segmental mobility of the polymer chains increases. After an optimal amount (15 wt% EC+PC), further increase in plasticizer content leads to re-crystallization of the system due to cross-linking of neighbouring polymer segments and hence a decrease in dispersion frequency is noted. Fig. 5.71 shows temperature response of dispersion frequency of PPSP system. Increase in temperature supports faster segmental motion of the polymer chains and hence the values of dispersion frequency increase linearly with increase in temperature.





Figs. 5.68(a-c) Dielectric response for various concentrations of EC+PC.

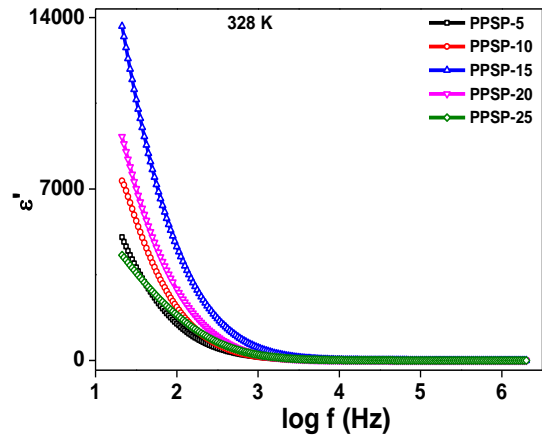


Fig. 5.69 Dielectric response of PPSP-system.

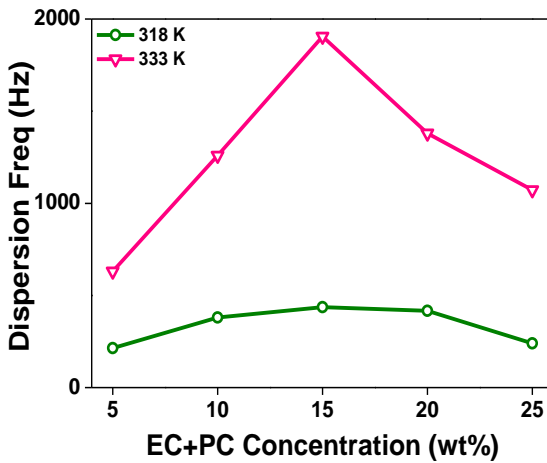


Fig. 5.70 Dispersion frequency as a function of EC+PC concentration.

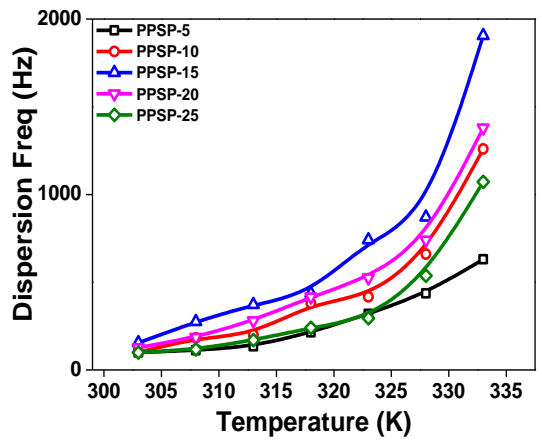
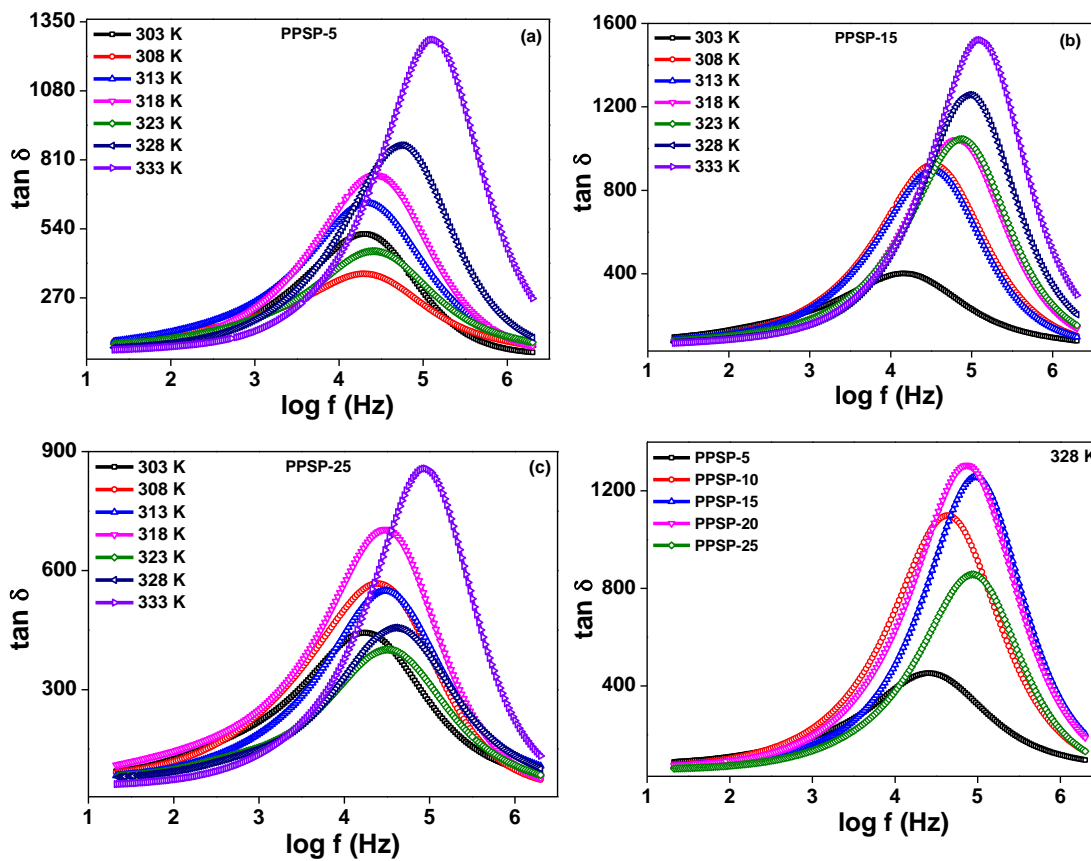


Fig. 5.71 Dispersion frequency as a function of temperature for PPSP-system.

Figs. 5.72(a-c) shows dielectric loss for various concentrations of EC+PC. Fig. 5.73 shows dielectric loss for PPSP system. The loss peaks shift towards higher frequency side up to PPSP-15 sample and then shift back to lower frequency side for PPSP-20 and PPSP-25 samples. A maximum value of $\tan \delta$ peaks is observed for PPSP-15 sample. The peak frequencies increase with increase in plasticizer content up to 15 wt% and then decrease after it (Fig. 5.74). The trend observed in all loss tangent plots above suggests that addition of plasticizers in the system leads to an increase in amorphocity of the system, enhancement in free volume and thereby an increase in mobility of the polymer segments (Hirankumar and Mehta, 2018) up to 15 wt% EC+PC content. Beyond 15 wt%, excess amount of plasticizer becomes a barrier for segmental motion and hence a decrease in loss frequencies is observed. Fig. 5.75 shows nature of peak frequencies of PPSP system with respect to temperature. Value of peak frequency

monotonically increases with increase in temperature as the increase in temperature favours polymer segmental mobility.



Figs. 5.72(a-c) Dielectric loss for various concentrations of EC+PC.

Figs. 5.73 Dielectric loss of PPSP-system.

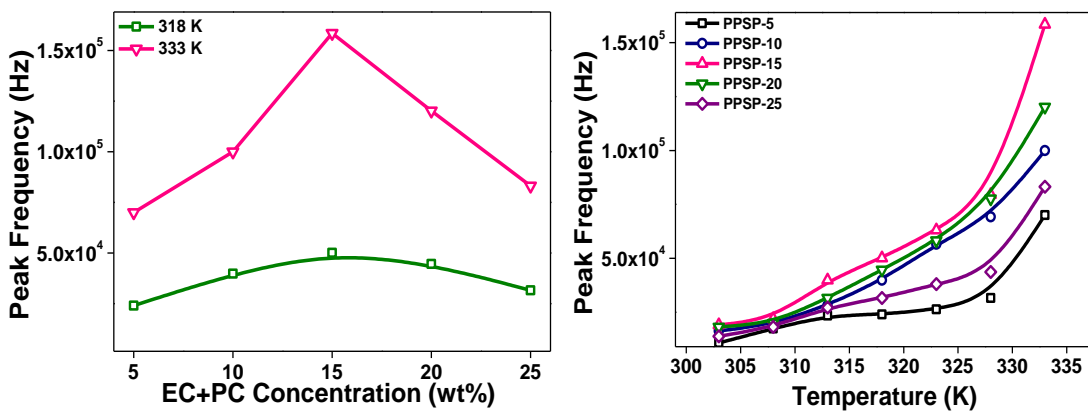


Fig. 5.74 Peak frequency as a function of EC+PC concentration.

Fig. 5.75 Peak frequency as a function of temperature for PPSP-system.

Effect of SHI on dielectric properties of plasticized blend polymer electrolytes

The irradiation effect on dielectric is shown in Fig. 5.76. The figure shows the dielectric response of PPSP-5 and PPSP-15 samples irradiated at various fluences. Characteristic nature of dielectric materials is followed by irradiated samples as well. Dispersion frequency values for PPSP-5 and PPSP-15 samples as a function of fluence is shown in Fig. 5.77. Dispersion frequency value increases with increase in fluence from 1×10^{11} ions/cm² to 1×10^{12} ions/cm² and decreases at 2×10^{12} ions/cm² fluence. Temperature response of PPSP-15 sample irradiated with fluence of 1×10^{12} ions/cm² is shown in Fig. 5.78. ϵ_r values increase linearly with increase in temperature and the effect can be vividly showcased in dispersion frequency versus temperature plots in Fig. 5.79.

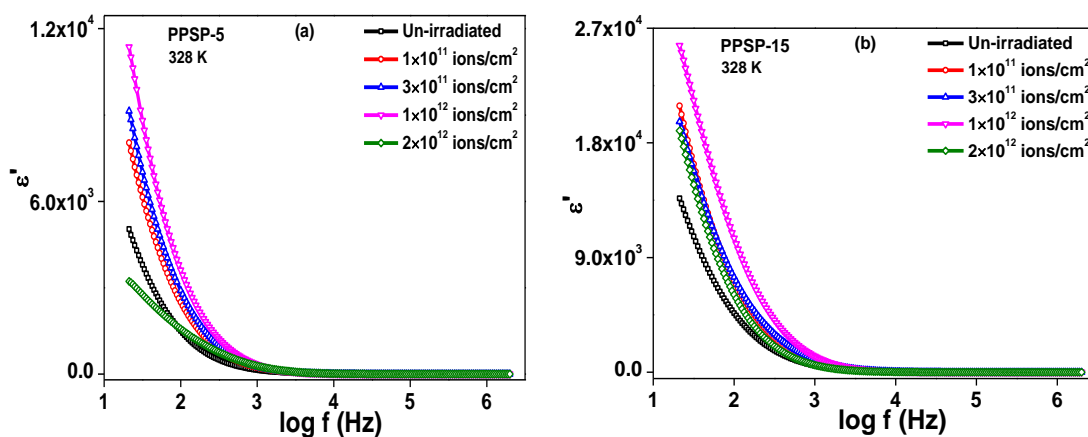


Fig. 5.76 Dielectric response of irradiated (a) PPSP-5 and (b) PPSP-15 samples.

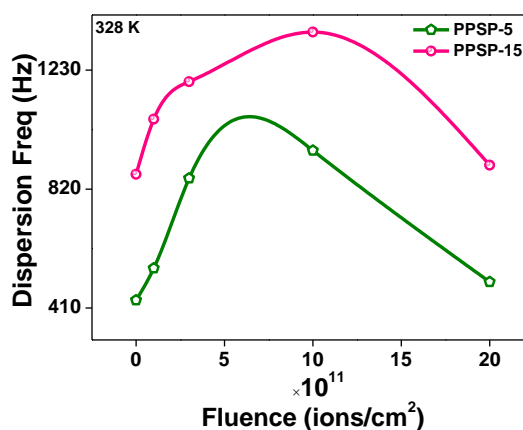


Fig. 5.77 Dispersion frequency as a function of fluence for PPSP-5 and 15 samples.

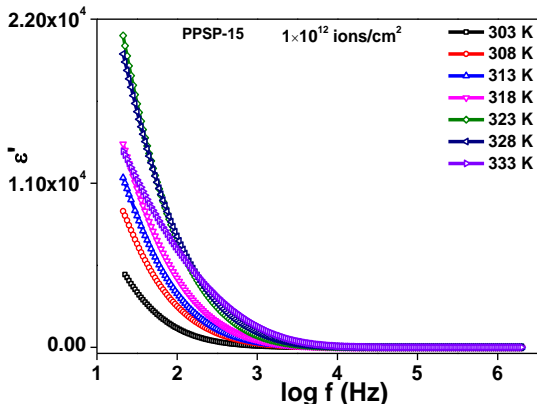


Fig. 5.78 Dielectric response of PPSP-15 sample irradiated at 1×10^{12} ions/cm² fluence.

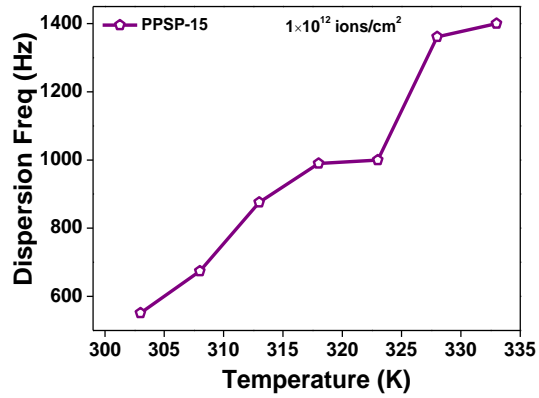


Fig. 5.79 Dispersion frequency of PPSP-15 sample irradiated at 1×10^{12} ions/cm² fluence.

Dielectric loss ($\tan \delta$) spectra of PPSP-5 and PPSP-15 samples at various fluences are plotted in Fig. 5.80(a) and (b). The peak frequency for irradiated PPSP samples increases towards high frequency side with increase in fluence up to 1×10^{12} ions/cm² and then decrease at 2×10^{12} ions/cm² fluence shown in Fig. 5.81. Dielectric loss for irradiated PPSP-15 sample with respect to temperature is shown in Fig. 5.82. The $\tan \delta$ peak values shift towards higher frequency side with increase in temperature and are plotted against temperature in Fig. 5.83. The loss peaks values increase continuously with increase in temperature. This is an expected trend in analogy with that observed in case of irradiated PPS samples.

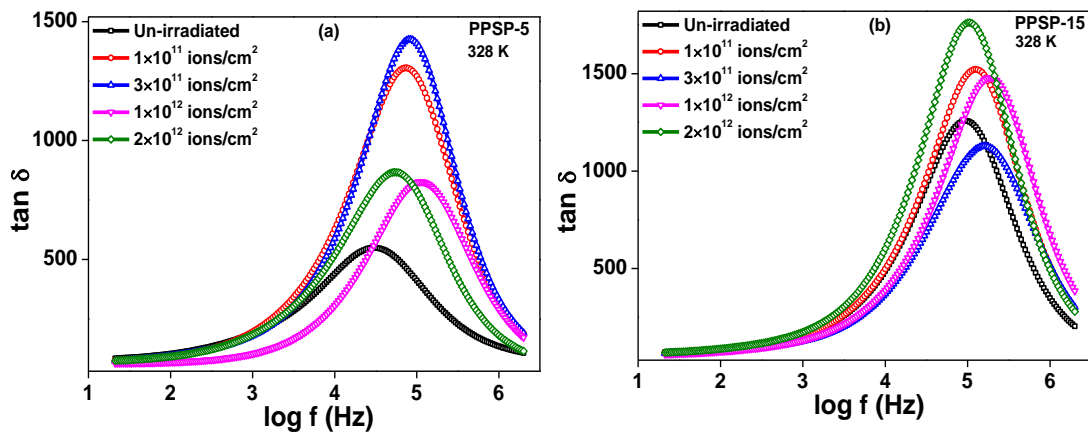


Fig. 5.80 Dielectric loss of irradiated (a) PPSP-5 and (b) PPSP-15 samples.

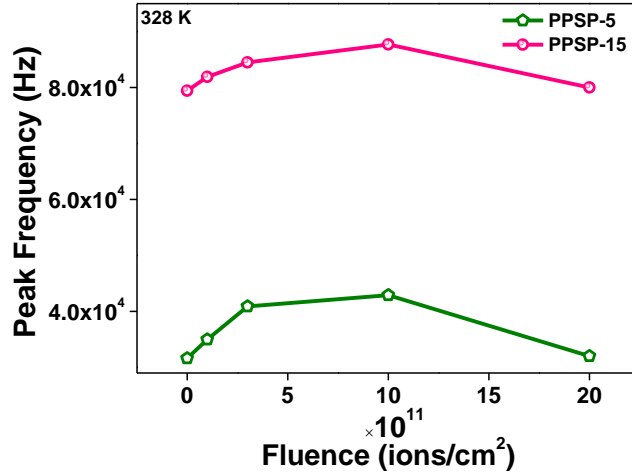


Fig. 5.81 Peak frequency as a function of fluence for PPSP-5 and 15 samples.

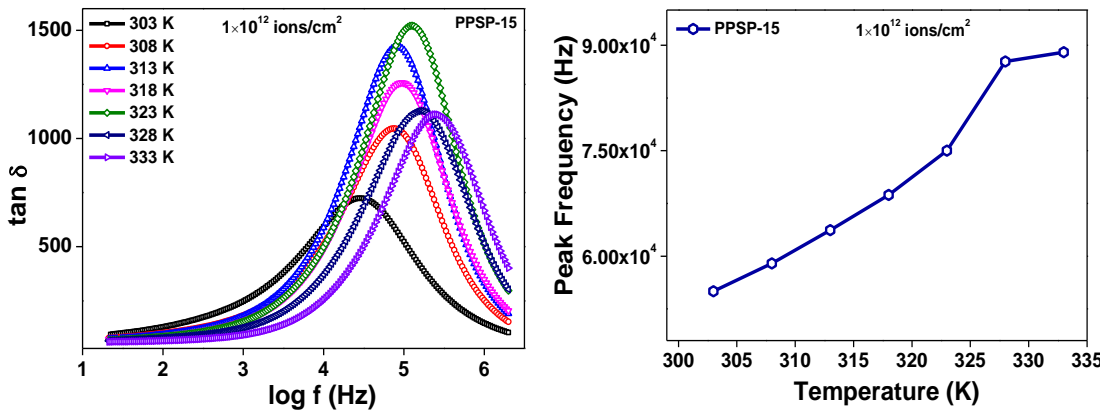
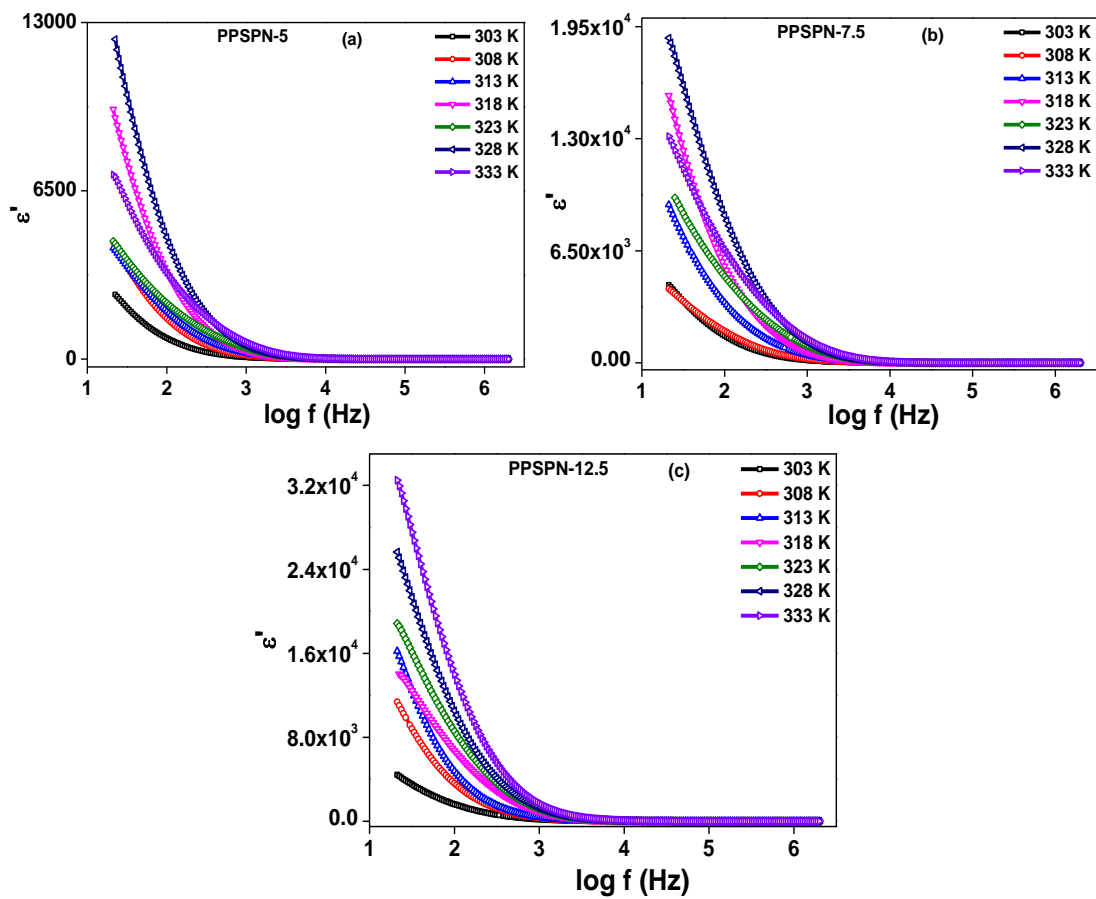


Fig. 5.82 Dielectric loss of PPSP-15 sample irradiated at 1×10^{12} ions/cm² fluence.

Fig. 5.83 Peak frequency of PPSP-15 sample irradiated at 1×10^{12} ions/cm² fluence.

Effect of SiO₂ on dielectric properties

Addition of inert nano-fillers in plasticized blend electrolytes showed further increase in ionic conductivity of the system. Hence it is important to understand the effect of nano-fillers on dielectric properties of the system. Fig. 5.84(a-c) shows dielectric behaviour of SPEs for various concentrations of SiO₂. Fig. 5.85 shows dielectric behaviour of PPSPN system. ϵ_r values increase for PPSPN-5 and PPSPN-7.5 samples, slightly decreases for PPSPN-10 sample, increases again for PPSPN-12.5 sample and finally decreases for PPSPN-15 sample. The dielectric shows maxima at PPSPN-12.5 sample. This pattern of the dielectric values with respect to SiO₂ content is perfectly traced by the dispersion frequency values as shown in Fig. 5.86. And Fig. 5.87 shows temperature variation of the dispersion frequency. The figure shows monotonic increase in dispersion frequency values as is expected and in analogy with PPS-system.



Figs. 5.84(a-c) Dielectric response for various concentrations of SiO_2 .

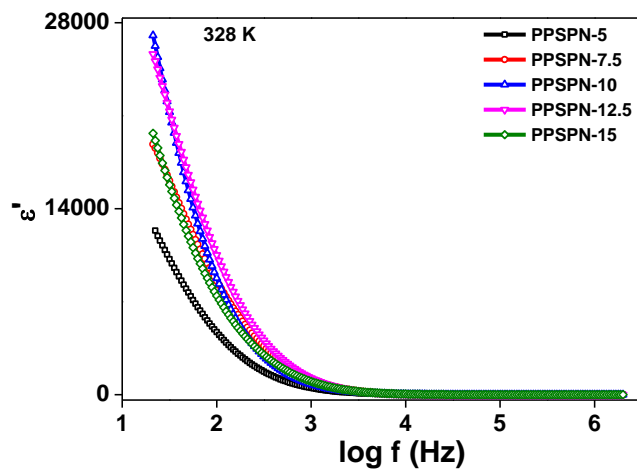


Fig. 5.85 Dielectric response of PPSPN-system.

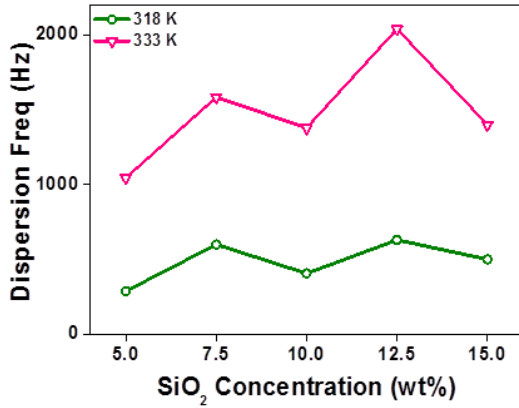


Fig. 5.86 Dispersion frequency as a function of SiO_2 concentration.

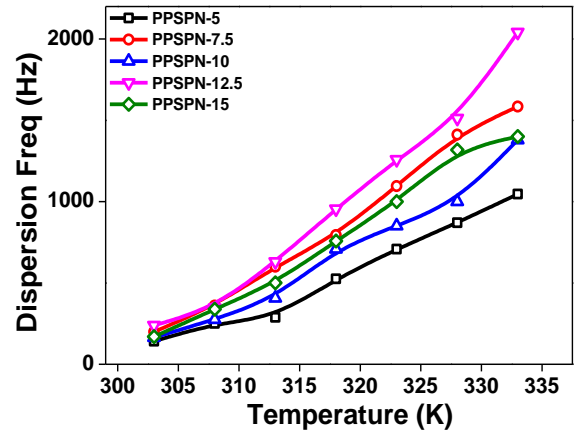
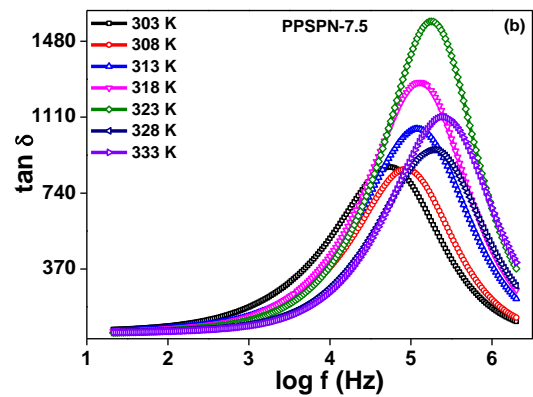
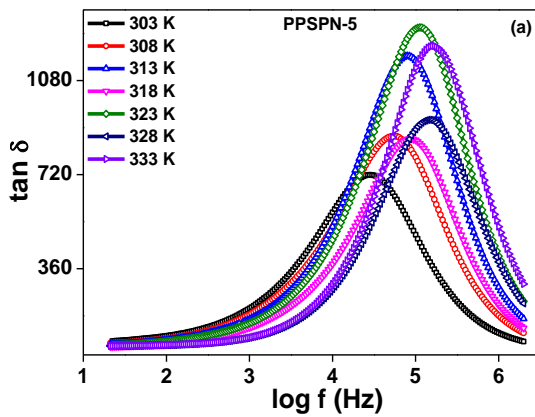
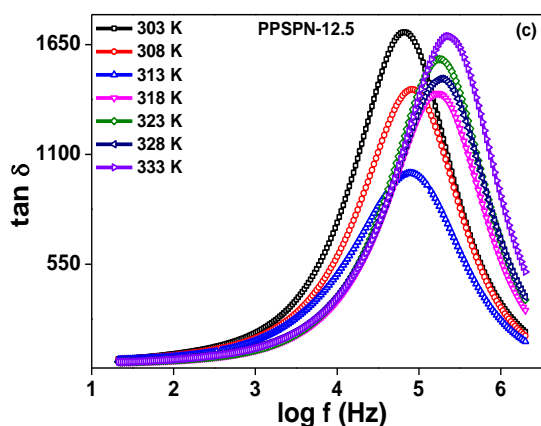


Fig. 5.87 Dispersion frequency as a function of temperature for PPSPN-system.

Dielectric loss for various concentrations of SiO_2 is plotted in Figs. 5.88(a-c) and Fig. 5.89 shows the dielectric loss for PPSPN system. $\tan \delta$ peak values also follow the trend outlined by dielectric values. The loss peaks shift towards higher frequency side for PPSPN-5 and PPSPN-7.5 samples and does not show any regular trend for higher percentage. Peak frequencies of PPSPN samples as function of SiO_2 concentration are plotted in Fig. 5.90. And Fig. 5.91 shows the peak frequencies with respect to temperature.





Figs. 5.88(a-c) Dielectric loss for various concentrations of SiO_2 .

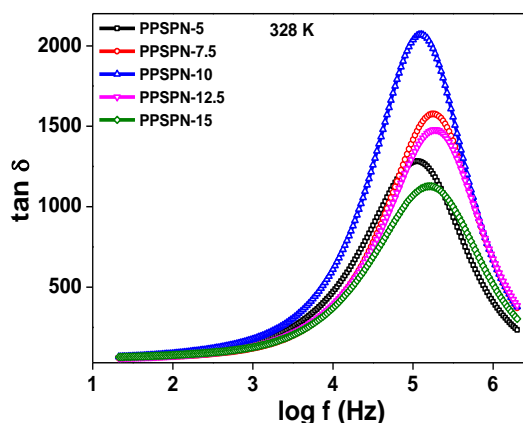


Fig. 5.89 Dielectric loss of PPSPN-system.

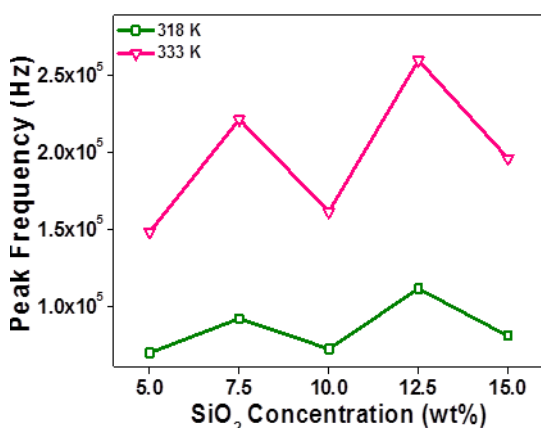


Fig. 5.90 Peak frequency as a function of SiO_2 concentration.

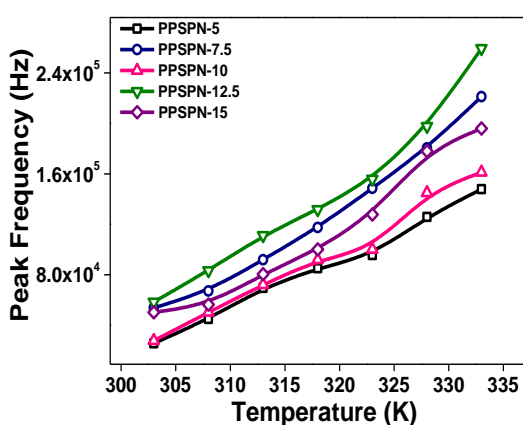


Fig. 5.91 Peak frequency as a function of temperature for PPSPN-system.

Effect of SHI on dielectric properties of nano-composite plasticized blend polymer electrolytes

The dielectric responses of PPSPN-7.5 and PPSPN-12.5 samples are recorded at various fluences and presented in Fig. 5.92 (a and b). ϵ_r values increase with fluence up to critical fluence value and then decrease for 2×10^{12} ions/cm² fluence. This effect is obvious from the dispersion frequency versus fluence plots for the irradiated samples as in Fig. 5.93. Fig. 5.94(a) shows dispersion frequency as a function of fluence for PPSPN-7.5 and 12.5 samples and dielectric response of irradiated PPSPN-12.5 sample is shown in Fig. 5.94(b). The dispersion frequency as a function of temperature for PPSPN-12.5 sample irradiated with 1×10^{12} ions/cm² fluence is plotted in Fig. 5.95. The ϵ_r values show tell-tale linear relationship with temperature as observed in case of un-irradiated samples.

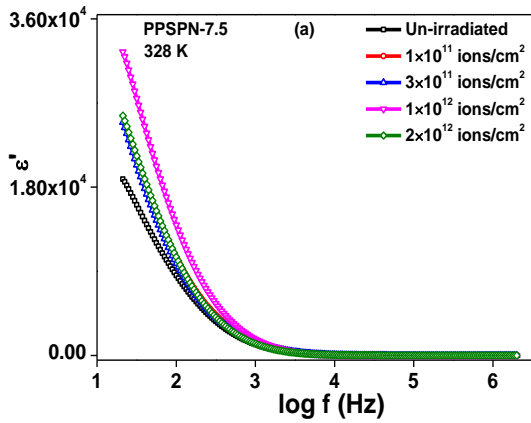


Fig. 5.92 Dielectric response of irradiated (a) PPSN-7.5 and (b) PPSN-12.5 samples.

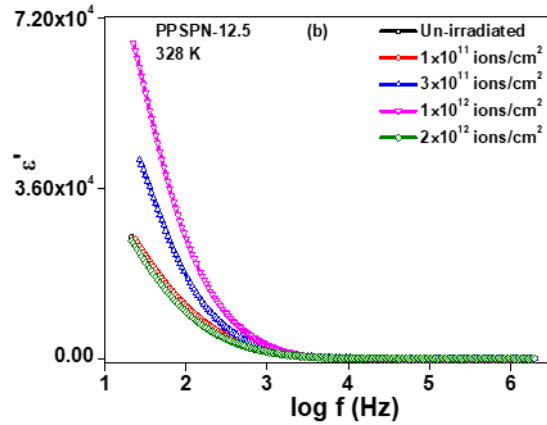


Fig. 5.93 Dispersion frequency as a function of fluence for PPSN-7.5 and 12.5 samples.

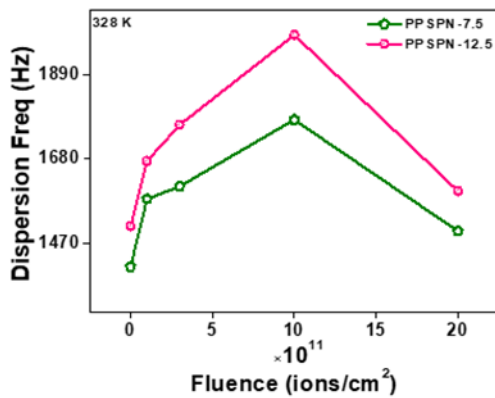


Fig. 5.94(a) Dispersion frequency as a function of fluence for PPSN 7.5 and 12.5 samples

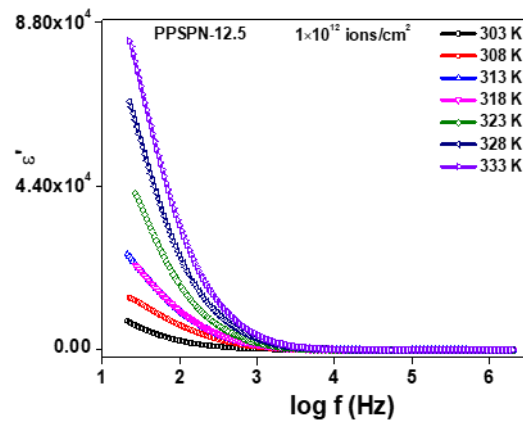


Fig. 5.94(b) Dielectric response of PPSN-12.5 sample irradiated at 1×10^{12} ions/cm² fluence

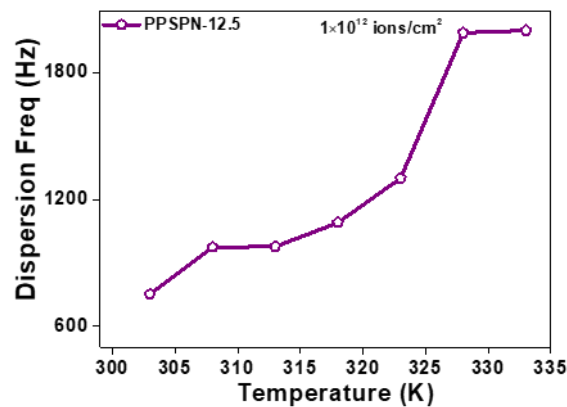


Fig. 5.95 Dispersion frequency of PPSN-12.5 sample irradiated at 1×10^{12} ions/cm² fluence.

Dielectric loss spectra of PPSPN-7.5 and PPSPN-12.5 samples irradiated with different fluences is shown in Fig. 5.96(a) and (b). The $\tan \delta$ peaks shift towards higher frequency side with increase in fluence up to 1×10^{12} ions/cm² fluence and then decreases at 2×10^{12} ions/cm² fluence. This effect very well manifests from the loss peak frequency versus fluence plots in Fig. 5.97. The variation in Loss tangent for irradiated PPSPN-12.5 sample at different temperatures is given in Fig. 5.98 and the linear increase in peak frequency with increase in temperature is clearly depicted in Fig. 5.99.

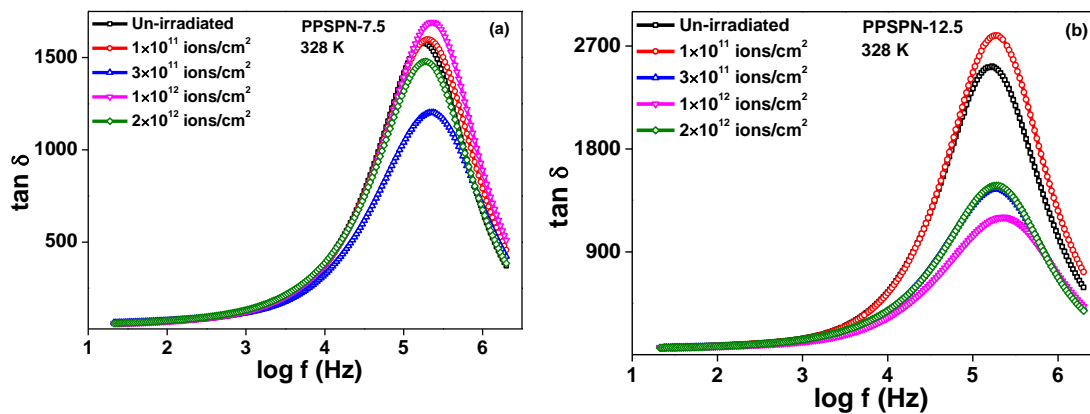


Fig. 5.96 Dielectric loss of irradiated (a) PPSPN-7.5 and (b) PPSPN-12.5 samples.

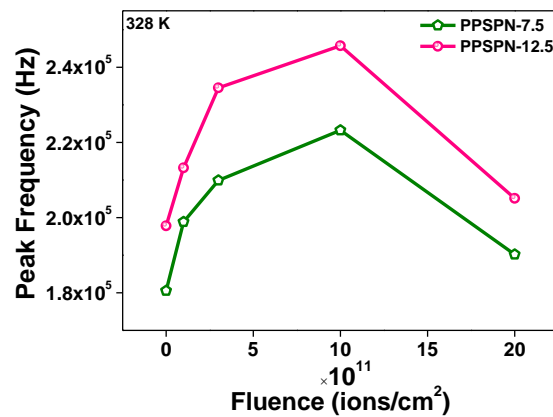


Fig. 5.97 Peak frequency as a function of fluence for PPSPN-7.5 and 12.5 samples.

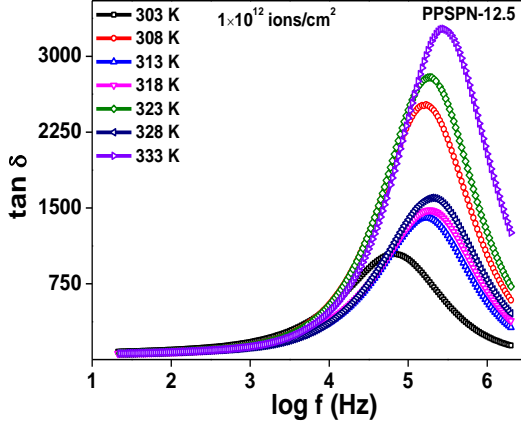


Fig. 5.98 Dielectric loss of PPSPN-12.5 sample irradiated at 1×10^{12} ions/cm² fluence.

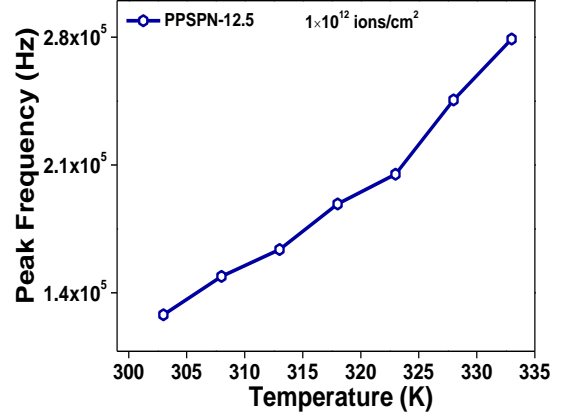


Fig. 5.99 Peak frequency of PPSPN-12.5 sample irradiated at 1×10^{12} ions/cm² fluence.

5.3 Modulus Formalism

The conductivity behaviour of ionic conductors can be well explained in terms of conductivity relaxation time τ , with the aid of modulus function M^* (Pradhan et al., 2008). Modulus formalism $M^*(\omega)$ is extracted from the complex permittivity through the following relationships (Hodge et al., 2005; Macedo et al., 1972; McCrum et al., 1991; Dam et al., 2016).

$$M^*(\omega) = \frac{1}{\varepsilon^*(\omega)} = j\omega C_0 Z^* = M'(\omega) + jM''(\omega)$$

$$= M_\infty \left[1 - \int_0^\infty \exp(-j\omega t) \left(\frac{d\varphi(t)}{dt} \right) dt \right] \quad (5.9)$$

where, M' and M'' are the real and imaginary parts of the complex modulus M^* . The function $\varphi(t)$ gives the time evolution of the electric field within the material and $\omega = 2\pi f$ is the angular frequency. Analysis of electrical relaxation in terms of complex permittivity $\varepsilon^*(\omega)$, gives relaxational parameters, characteristics of the decay of the displacement vector \vec{D} . The expression for the decay of electric field in time domain can be written as:

$$\vec{E}(t) = \vec{E}(0)\varphi(t) \quad (5.10)$$

where $\vec{E}(0)$ denotes the electric field at time $t = 0$ and $\varphi(t)$ is a macroscopic decay function of the general form

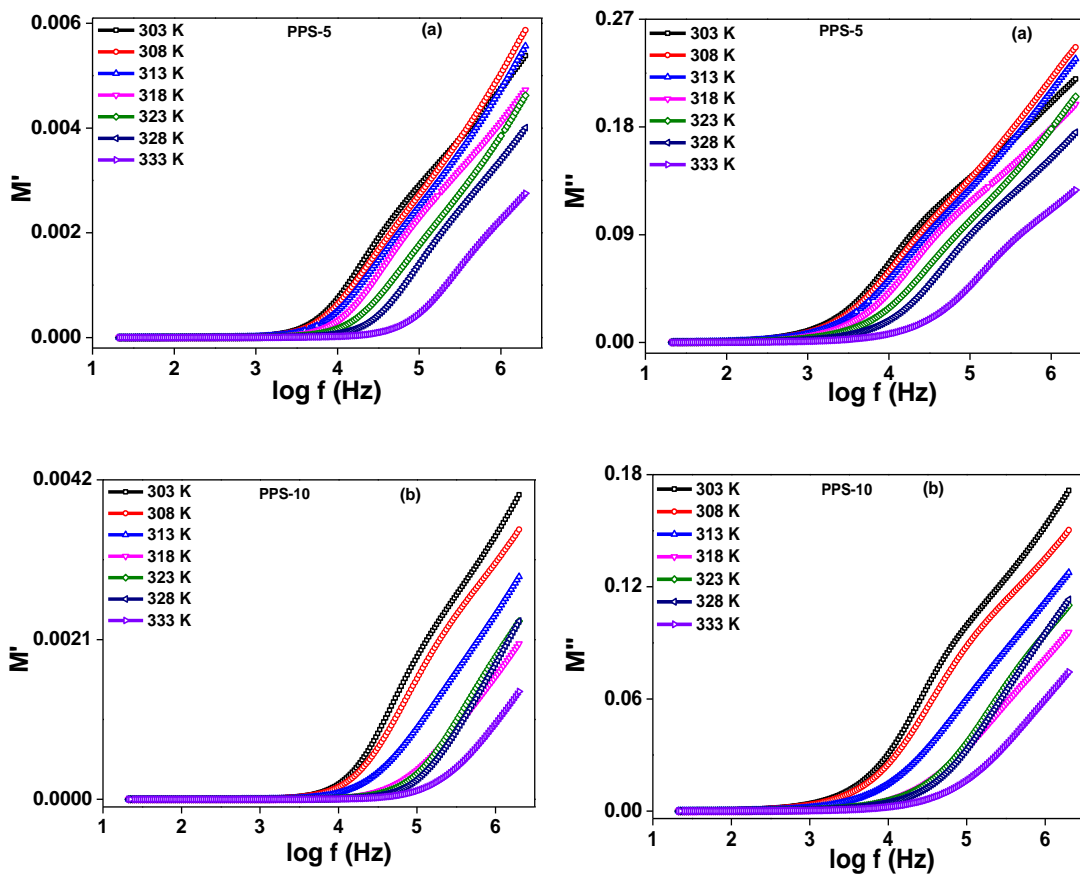
$$\varphi(t) = \int_0^\infty g(\tau_\sigma) \exp \left[-\left(\frac{t}{\tau_\sigma} \right)^\beta \right] dt \quad (5.11)$$

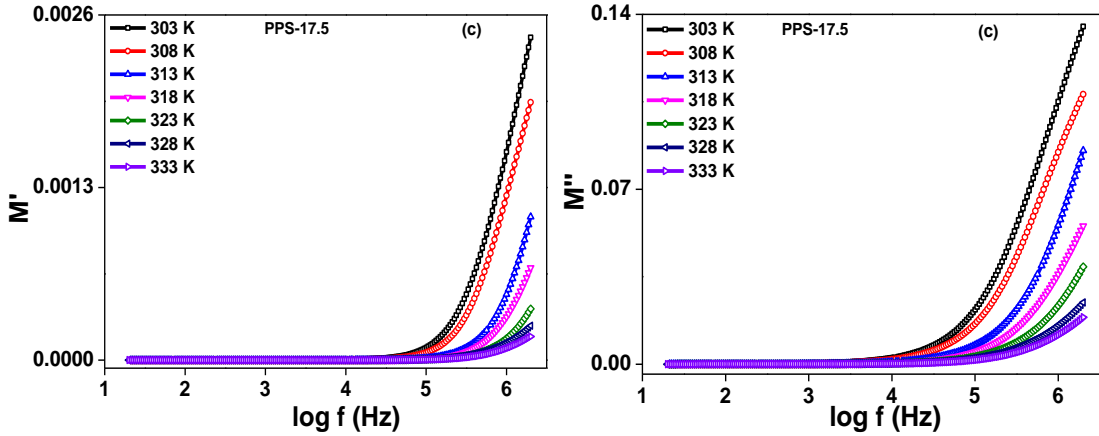
where τ_σ is conductivity relaxation time and $g(\tau_\sigma)$ is a normalized density function for relaxation times. Thus, using equations (5.10) and (5.12), we have,

$$M^*(\omega) = M_\infty \int_0^\infty g(\tau_\sigma) \left[\frac{j\omega\tau_\sigma}{1+j\omega\tau_\sigma} \right] d\tau_\sigma \quad (5.12)$$

Effect of NaCF₃SO₃ on modulus behaviour

Figs. 5.100 (a) to (c) show the real and imaginary values of modulus at different temperatures of all PPS samples and Fig. 5.101 shows the real and imaginary values of modulus behavior of PPS system at different salt concentration. There is a long tail appearing in the low frequency region for both real and imaginary modulus functions and the modulus plots shift towards higher frequency side with increase in temperature. The appearance of long tail is attributed to the large capacitance in M'' associated with the electrode polarization phenomenon, which is quiet pronounced at lower frequencies (Pant et al., 2009). The presence of long tails in the lower frequency region of modulus function also confirms the evidence of non-Debye nature (Ibrahim et al., 2012). Relaxation peaks in M'' are not observed in the modulus spectra.





Figs. 5.100(a-c) Modulus behaviour of various concentrations of NaCF_3SO_3 .

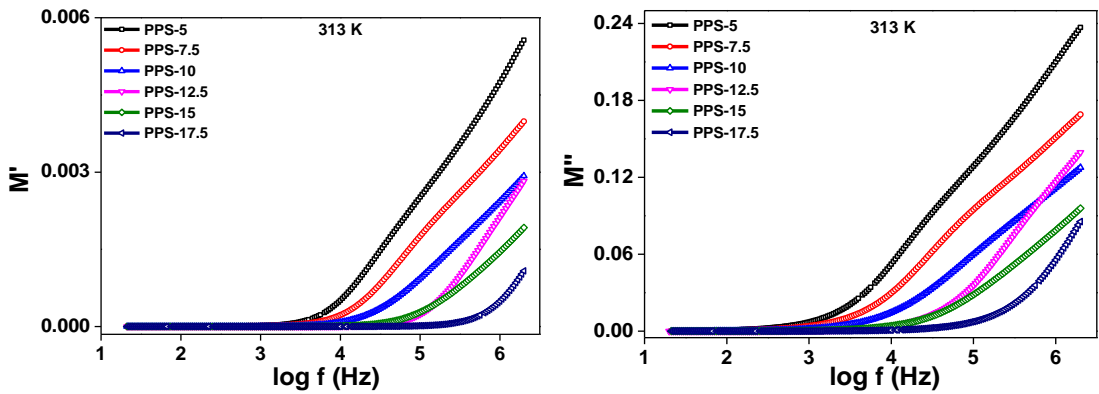


Fig. 5.101 Modulus behaviour of PPS-system.

Modulus behavior has, therefore, been interpreted using the frequency values from where the relaxation phenomenon sets on. Fig. 5.102 shows onset frequency as a function of concentration and Fig. 5.103 shows temperature dependence of the onset frequency. With increase in salt concentration and temperature, the onset frequency of modulus spectra shifts towards higher frequency side. This suggests that the relaxation time decreases with increase in salt concentration and temperature. This increase in onset frequency (decrease in relaxation time) is extensively used for analyzing the conductivity process (Pradhan *et al.*, 2008). This variation in frequency with salt concentration and temperature is in consonance with the conductivity and the dielectric constant in PPS system.

Effect of SHI on modulus behaviour of blend polymer electrolytes

After irradiation, modulus behavior of PPS-7.5 and PPS-17.5 samples are shown in Figs. 5.104 (a) and (b). The plots show that the values of M' and M'' shift towards higher

frequency side with increase in fluence upto 1×10^{12} ions/cm² (critical fluence value) and then shift is reversed towards low frequency at 2×10^{12} ions/cm² fluence. The onset frequency versus fluence plot is shown in Fig. 5.105. The shift in onset frequency with increase in fluence may be due to the release of increased number of trapped charge carriers and their long-range hopping explained by Raghu et al. (2014). Behaviour of modulus function with respect to temperature at critical fluence value is also plotted in Fig. 5.106 and the modulus values shift towards higher frequency side continuously with rise in temperature. Temperature profile of onset frequency for PPS-17.5 sample irradiated at 1×10^{12} ions/cm² fluence is plotted in Fig. 5.107. This nature of the onset frequency and the relaxation times is in accordance with the conductivity and dielectric constant behavior of irradiated PPS samples.

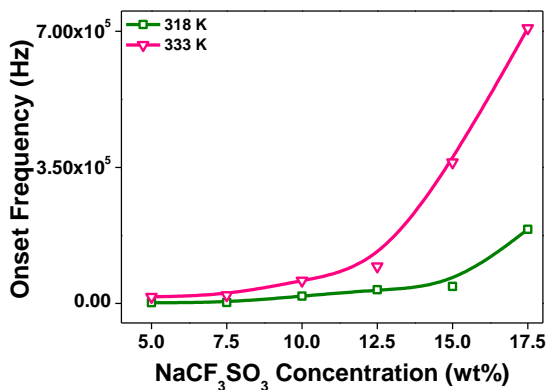


Fig. 5.102 Onset frequency as a function of NaCF_3SO_3 concentration.

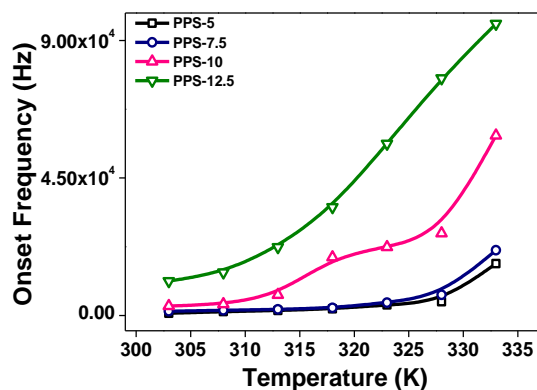
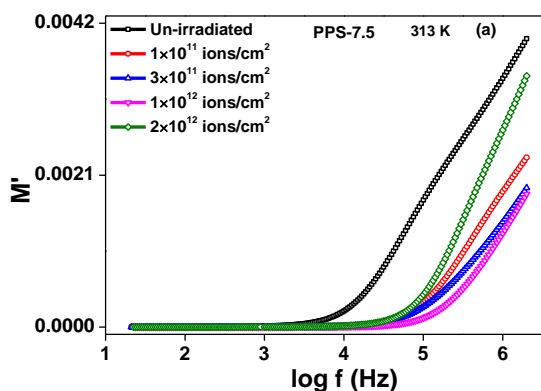
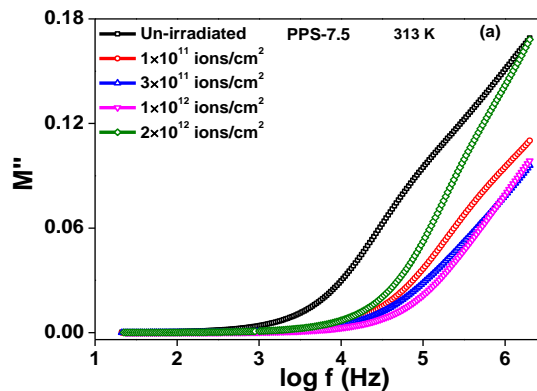
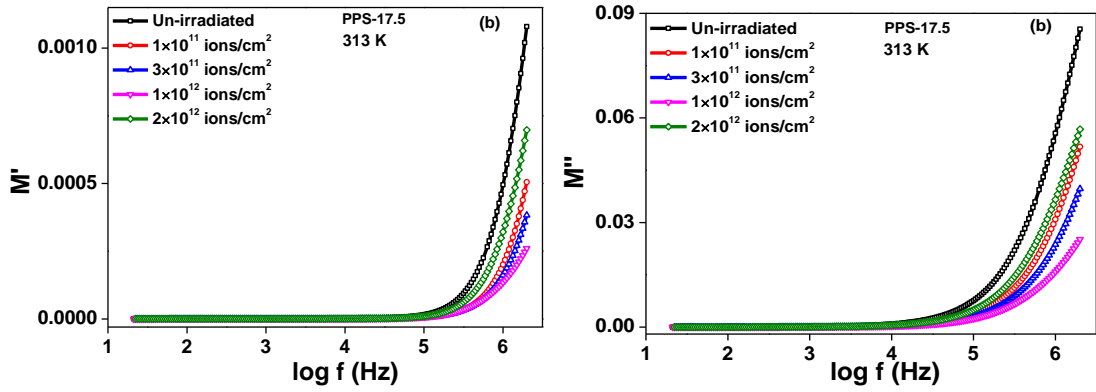


Fig. 5.103 Onset frequency as a function of temperature for PPS-system.



Figs. 5.104(a) Modulus behavior of irradiated PPS-7.5 samples.





Figs. 5.104(b) Modulus behavior of irradiated PPS-17.5 samples.

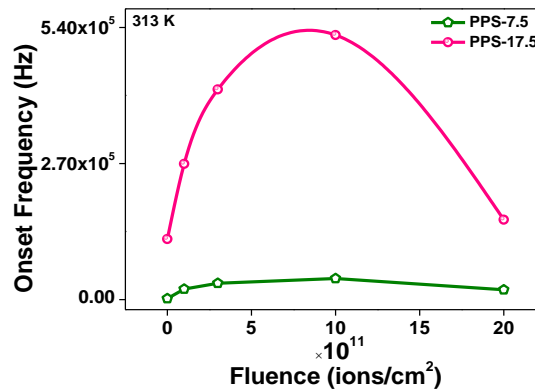


Fig. 5.105 Onset Frequency as a function of fluence for PPS-7.5 and 17.5 samples.

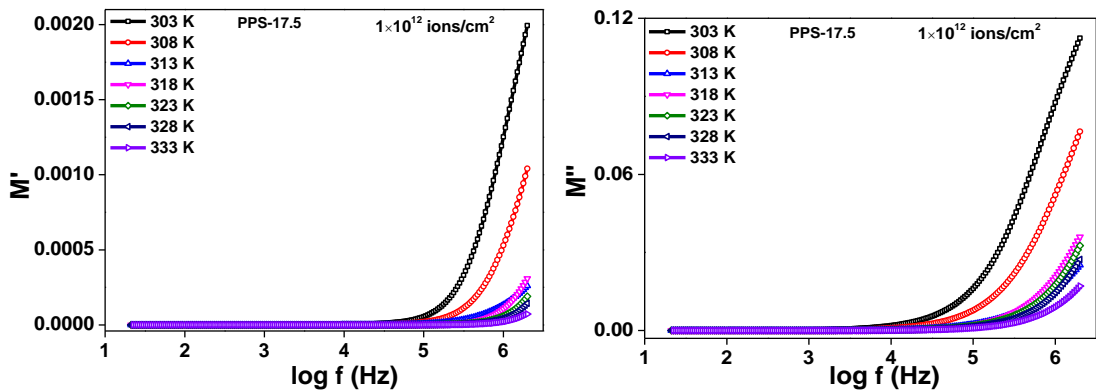


Fig. 5.106 Modulus behavior of irradiated PPS-17.5 sample at different temperatures.

Effect of plasticizers (EC+PC) on modulus behaviour

After conductivity, it was observed that the dielectric properties of the electrolyte system also showed a reasonable increase by addition of plasticizers in the system, it is thus important to support our findings with respect to modulus behavior as well. **Figs. 5.108(a-c)** show the real values M' and imaginary M'' modulus of various samples of PPSP system and **Fig. 5.109** shows variation of real M' and imaginary M'' values of modulus with frequency f of all PPSP films. In case of plasticizer also, a long tail in the

lower frequency region is observed and as the temperature rises, modulus plots shift towards higher frequency side. Fig. 5.110 shows how onset frequency as a function of EC+PC concentration changes when plasticizer is added.

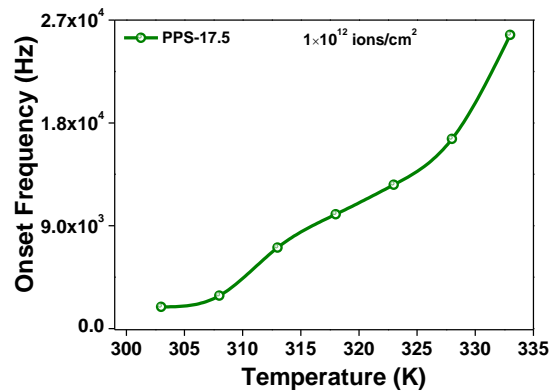
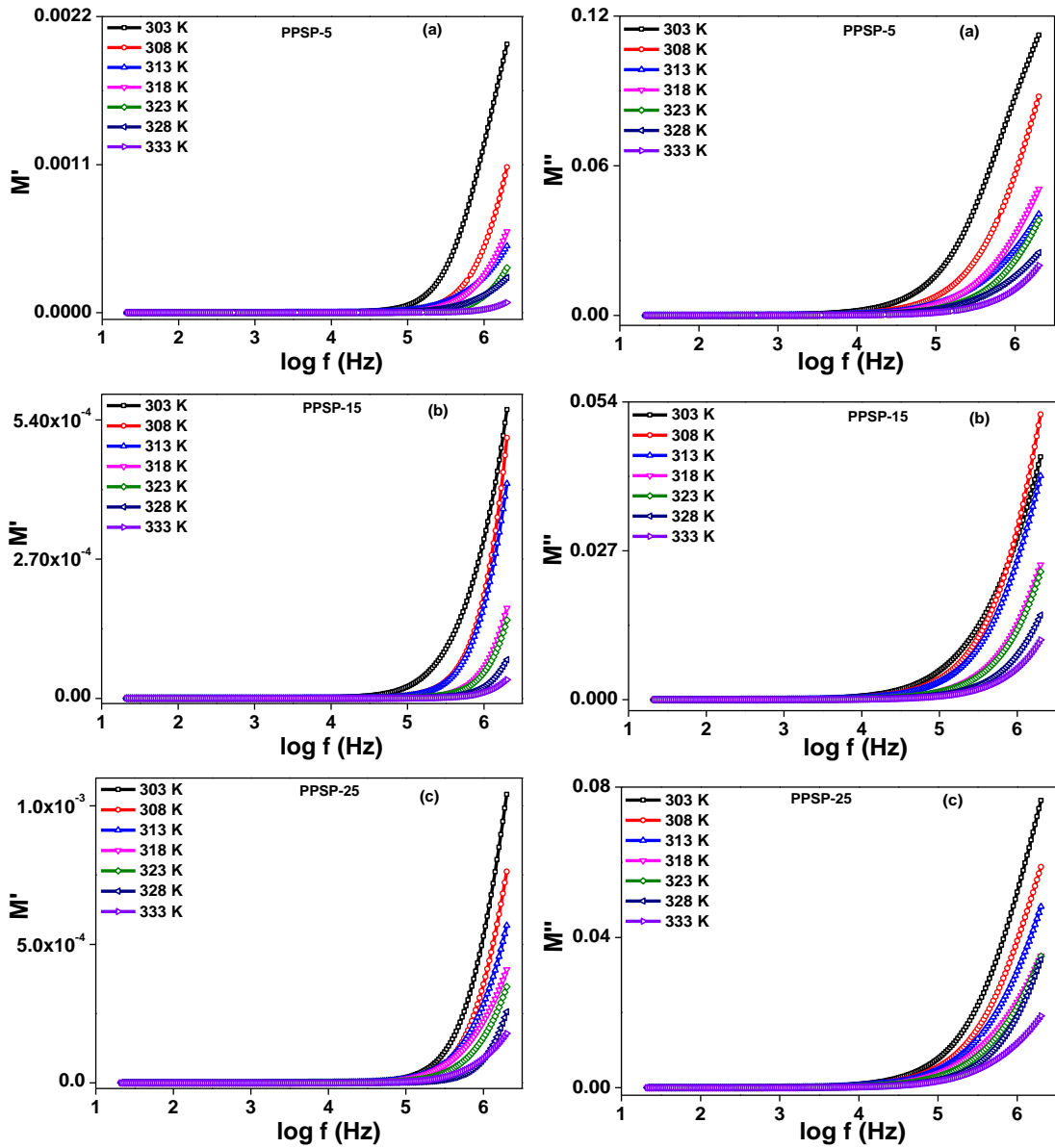


Fig. 5.107 Onset Frequency as a function of temperature for PPS-17.5 sample irradiated at 1×10^{12} ions/cm² fluence.

With increase in EC+PC concentration, the onset frequency of relaxation increases from PPSP-5 sample to PPSP-15 sample and then decreases for PPSP-20 and PPSP-25. The temperature dependence of the onset frequency is depicted in Fig. 5.111. The onset frequency increases with increase in temperature and this behaviour of the onset frequency of PPSP samples is in good agreement with its conductivity and dielectric behaviour.

Effect of SHI on modulus behaviour of plasticized blend polymer electrolytes

Now the modulus behavior of PPSP-5 and PPSP-15 samples at different fluences are shown in Figs. 5.112(a) and (b). Here also, the modulus plots shift towards higher frequency side with increase in fluence up to 1×10^{12} ions/cm² and a long tail in the lower frequency region for both real and imaginary modulus functions is observed. The onset frequency values of the irradiated samples at different fluences are given in Fig. 5.113. The onset frequency also shifts to high frequency side with fluence and then shifts to lower frequency side at highest fluence. The temperature effect of Modulus on irradiated PPSP-15 sample at 1×10^{12} ions/cm², is plotted in Fig. 5.114 and the onset frequency behaviour with respect to temperature is plotted in Fig. 5.115. The onset frequency rises with rise in temperature linearly and the variation in relaxation time is in consonance with the conductivity and dielectric constant of irradiated PPSP samples.



Figs. 5.108(a-c) Modulus behaviour of various concentrations of EC+PC.

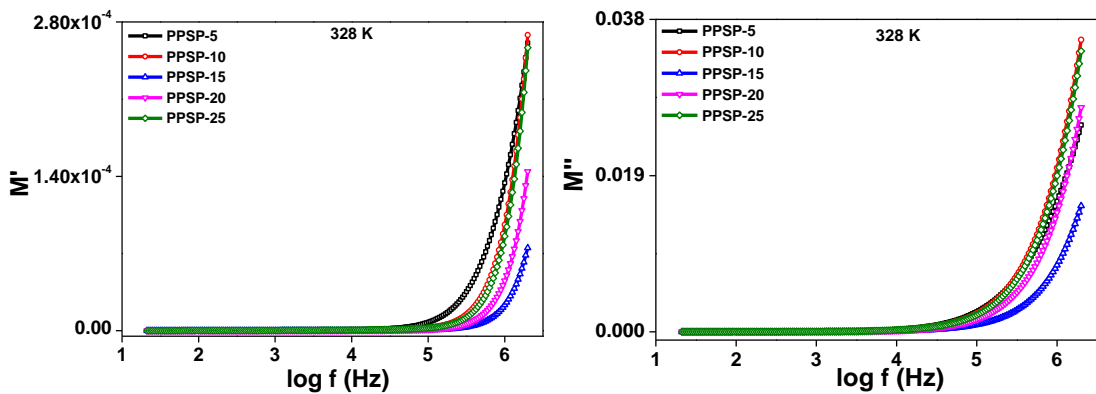


Fig. 5.109 Modulus behaviour of PPSP system.

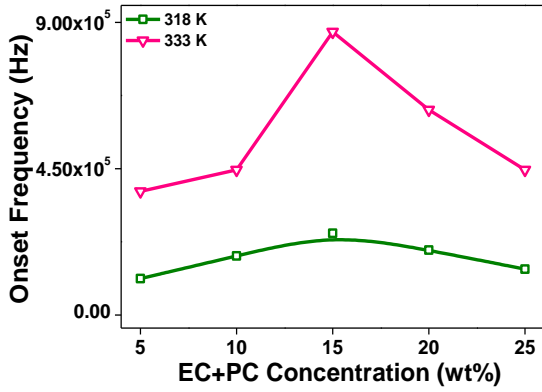


Fig. 5.110 Onset frequency as a function of EC+PC concentration.

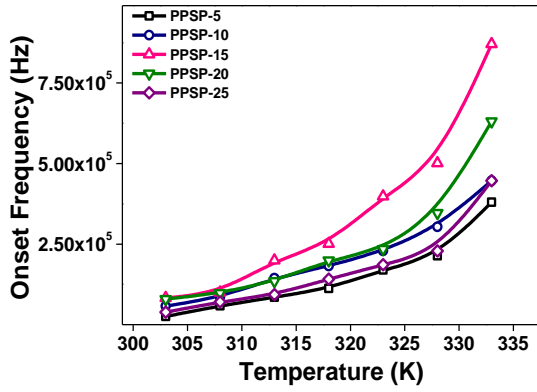
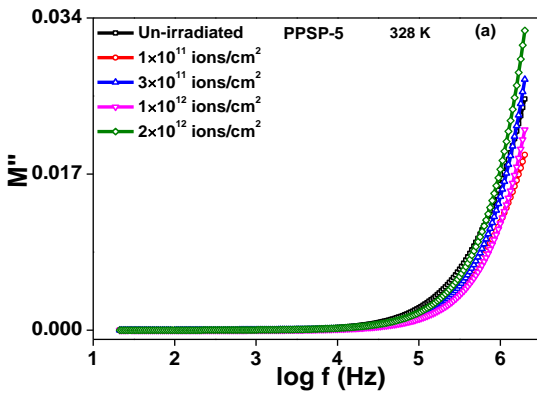
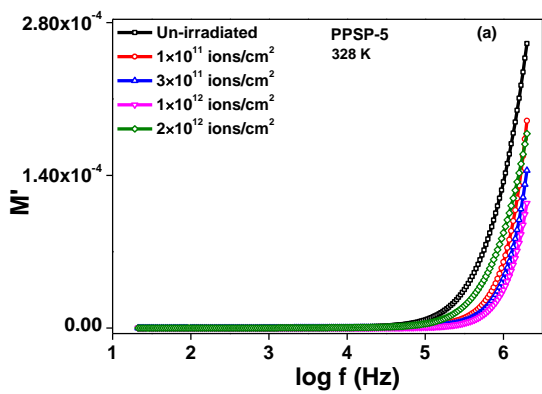
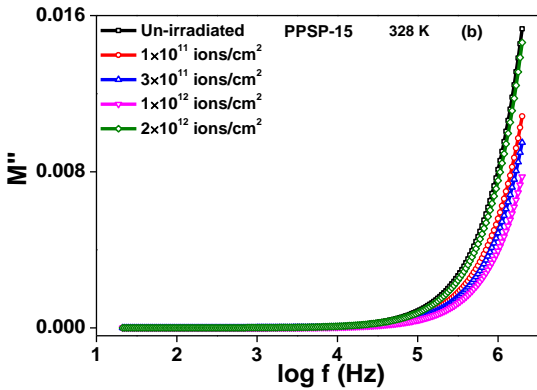
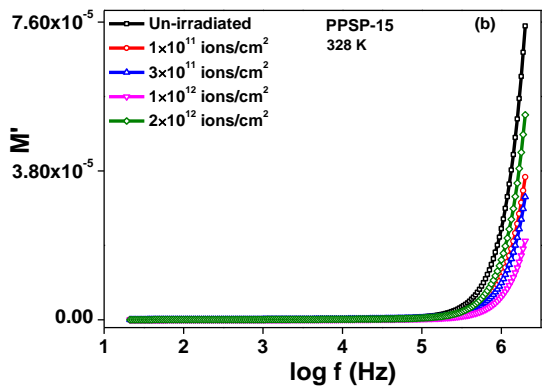


Fig. 5.111 Onset frequency as a function of temperature for PPSP-system.



Figs. 5.112(a) Modulus behavior of irradiated PPSP-5 sample.



Figs. 5.112(b) Modulus behavior of irradiated PPSP-15 sample.

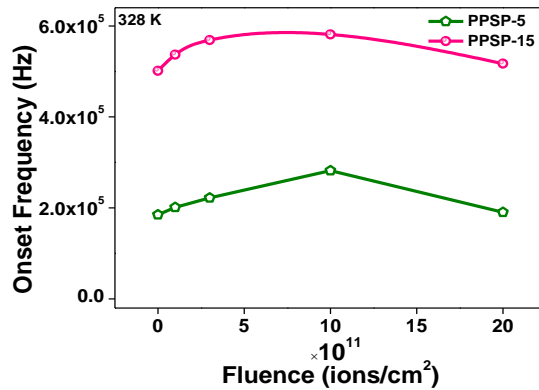


Fig. 5.113 Onset Frequency as a function of fluence for PPSP-5 and 15 samples.

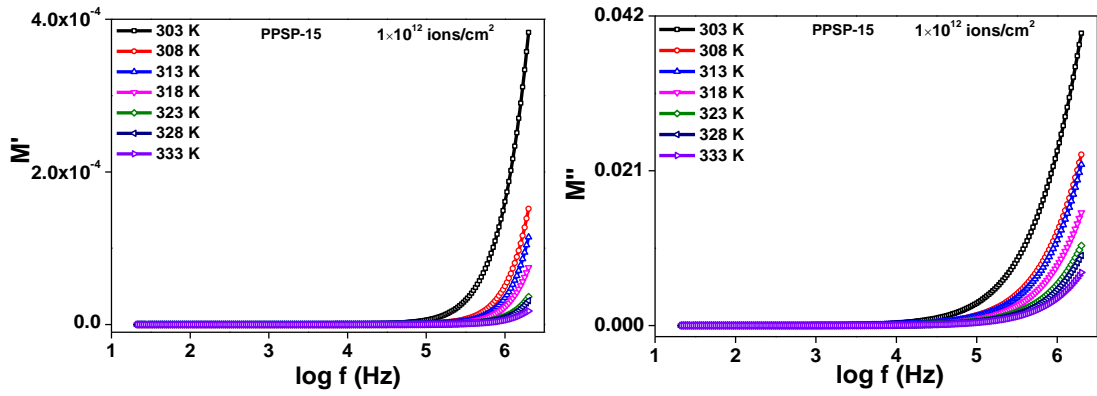


Fig. 5.114 Modulus behavior of irradiated PPSP-15 sample at different temperatures.

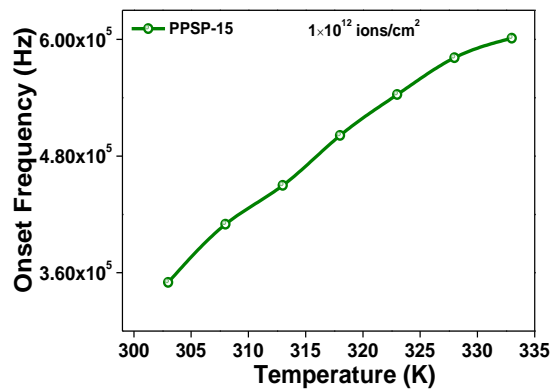
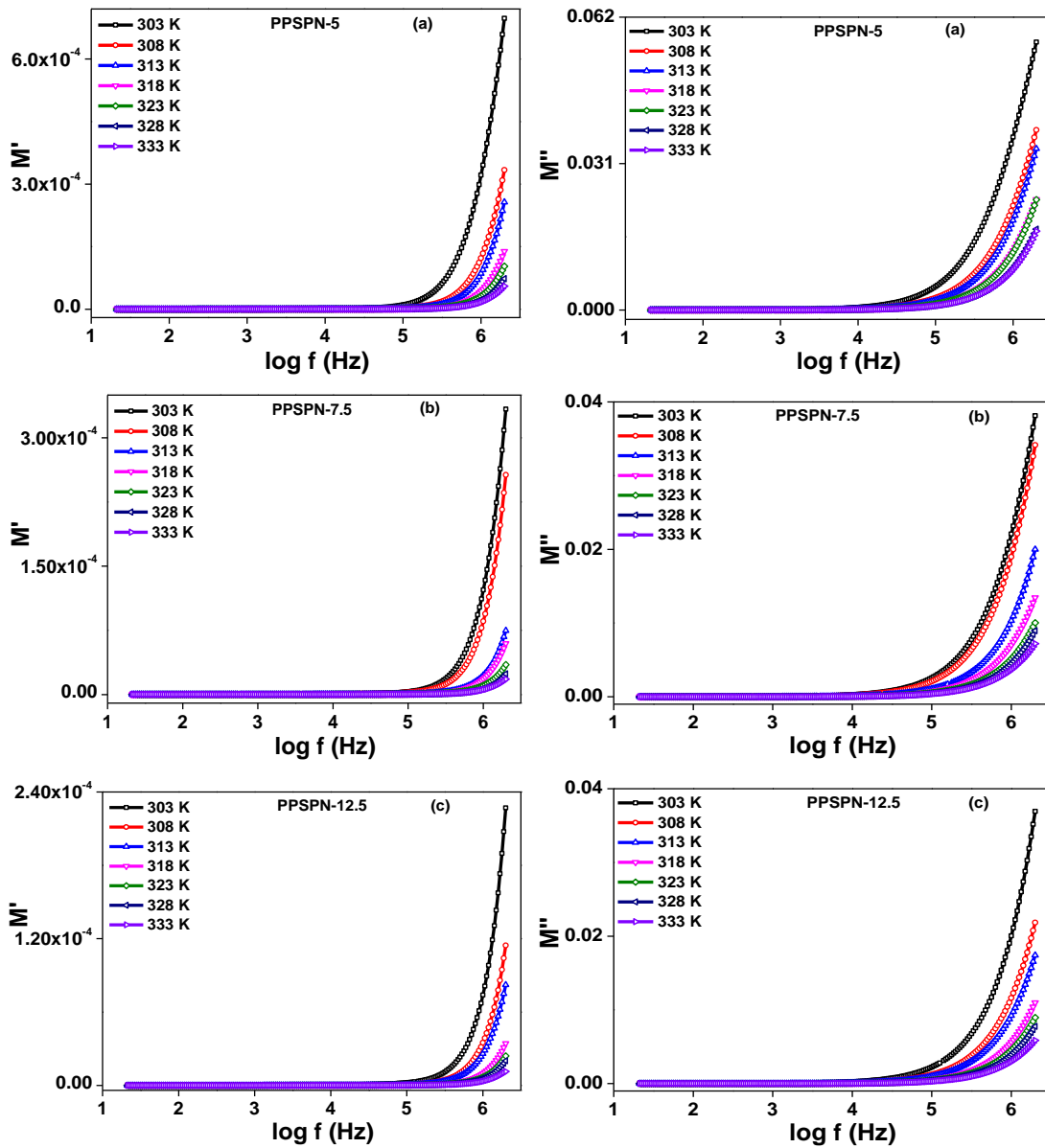


Fig. 5.115 Onset Frequency as a function of temperature for PPSP-15 sample irradiated at 1×10^{12} ions/cm² fluence.

Effect of SiO₂ on modulus behaviour

Finally, incorporation of inert nano-filler (SiO₂), particles in the plasticized electrolyte system led to an enhancement in conductivity and dielectric properties of the system. We study the modulus properties of the nano-filler dispersed samples also. Figs. 5.116(a-c) show the real and imaginary values of modulus of various samples of PPSPN system and Fig. 5.117 shows variation of modulus (real and imaginary) of all PPSPN system with frequency. Plots of modulus function shift towards higher frequency side with increase in temperature and the characteristic long tail appears at lower frequencies for all the plots.



Figs. 5.116(a-c) Modulus behaviour of various concentrations of SiO_2 .

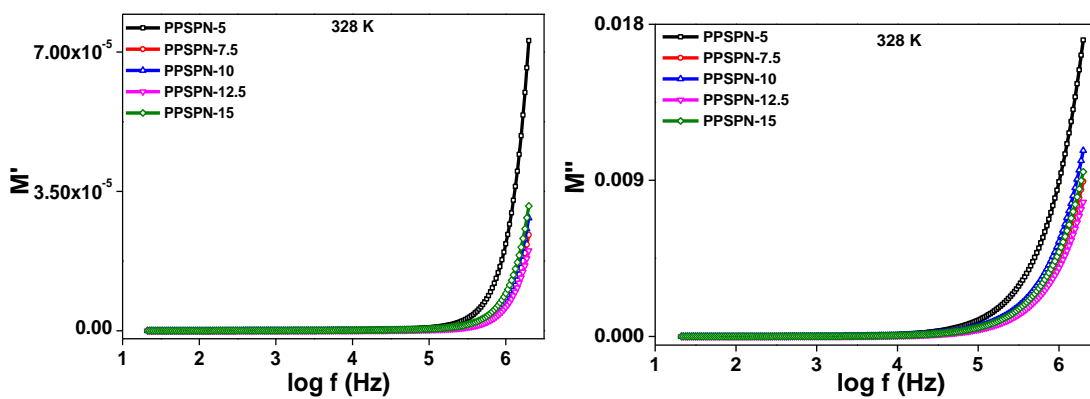


Fig. 5.117 Modulus behaviour of PPSN system.

The variation of onset frequency with respect to SiO₂ concentration is shown in Fig. 5.118. Modulus function shows maxima for PPSPN-7.5 and 12.5 sample. Fig. 5.119 shows variation of onset frequency values for PPSPN samples with respect to temperature. The values increase with temperature for all samples with nano-filler dispersed in them.

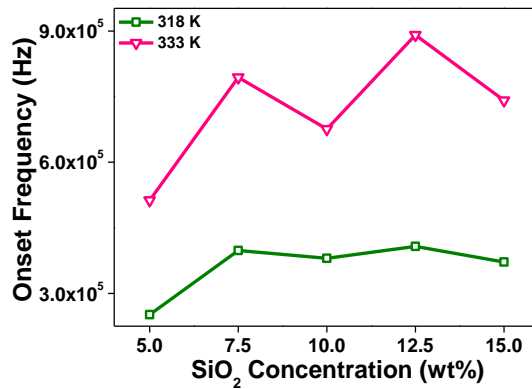


Fig. 5.118 Onset frequency as a function of SiO₂ concentration.

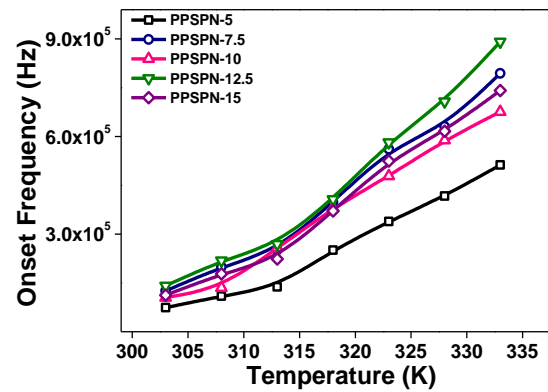
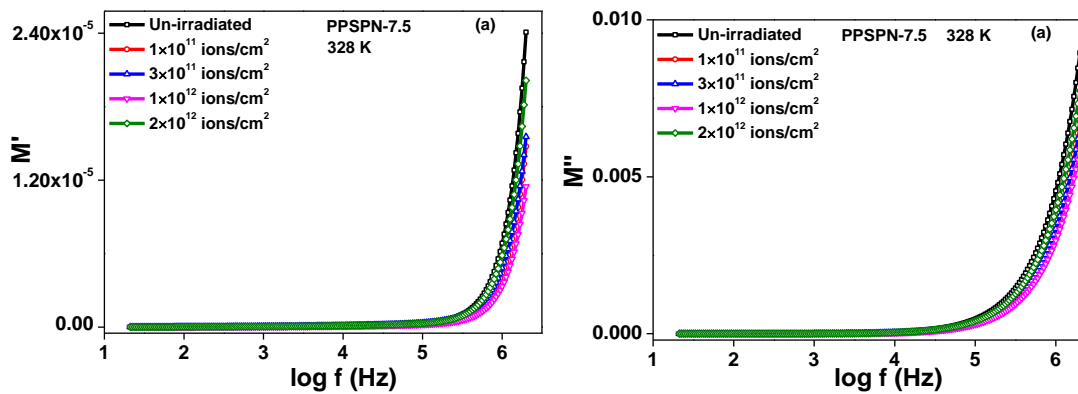


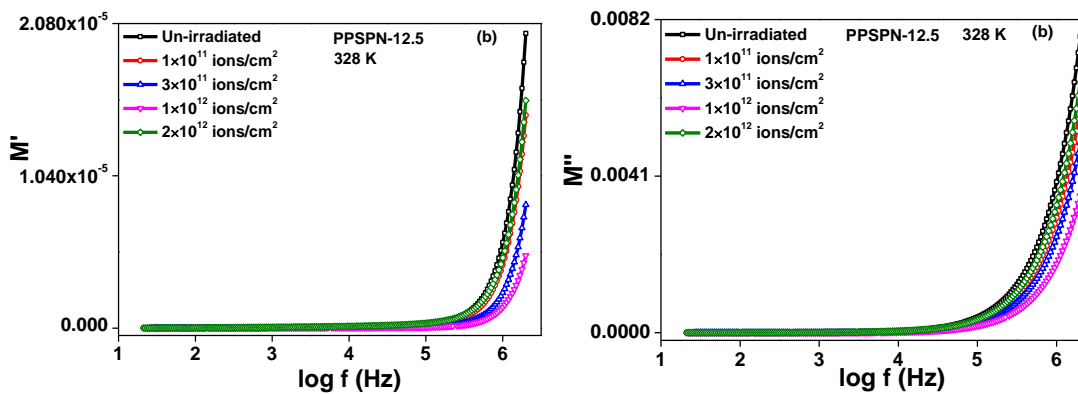
Fig. 5.119 Onset frequency as a function of temperature for PPSPN-system.

Effect of SHI on modulus behaviour of nano composite plasticized blend polymer electrolytes

Figs. 5.120 (a) and (b) show real and imaginary values of modulus of PPSPN-7.5 and PPSPN-12.5 samples irradiated at various fluences. M' and M'' plots shift towards higher frequency side with increase in fluence up to 1×10^{12} ions/cm² which show a long tail in the lower frequency region. The variation of onset frequency values with respect to fluence of two samples are shown in Fig. 5.121. The increase of onset frequency up to 1×10^{12} ions/cm² fluence and then decrease is on expected lines. Fig. 5.122 shows temperature response of Modulus (Real and Imaginary) of irradiated PPSPN-12.5 sample at 1×10^{12} ions/cm² fluence and Fig. 5.123 shows temperature profile of the corresponding onset frequency of irradiated PPSPN-12.5 sample at 1×10^{12} ions/cm² fluence.



Figs. 5.120(a) Modulus behavior of irradiated PPSPN-7.5 samples.



Figs. 5.120(b) Modulus behavior of irradiated PPSPN-12.5 samples.

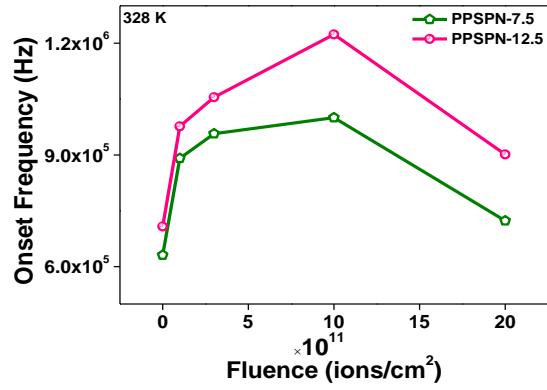


Fig. 5.121 Onset Frequency as a function of fluence for PPSPN-7.5 and 12.5 samples.

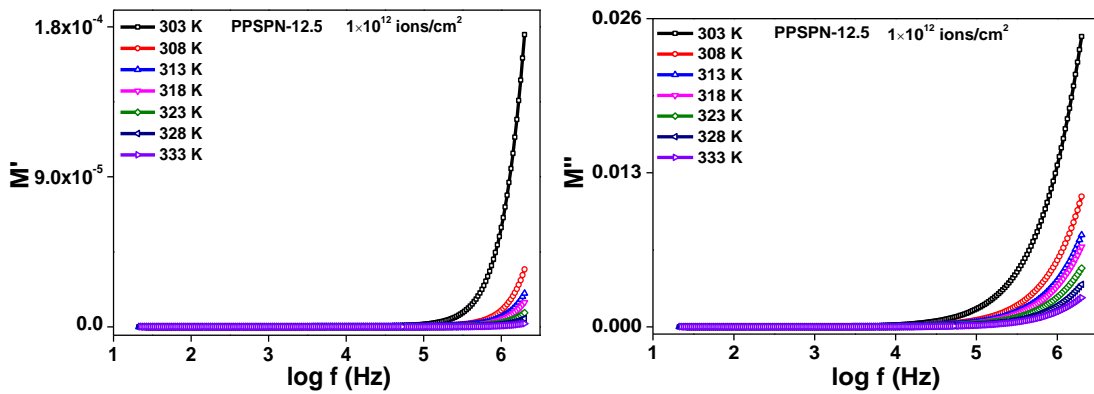


Fig. 5.122 Modulus behavior of irradiated PPSPN-12.5 sample at different temperatures.

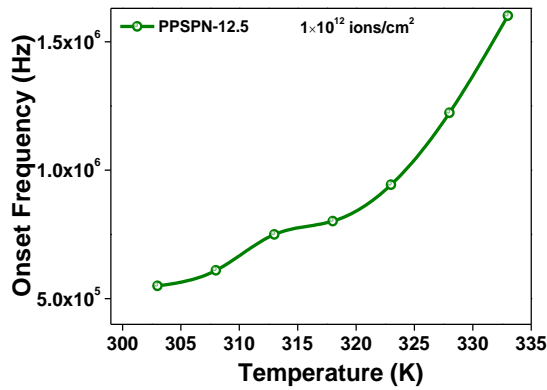


Fig. 5.123 Onset Frequency as a function of temperature for PPSPN-12.5 Sample irradiated at 1×10^{12} ions/cm² fluence.

It is widely clear from the graphs that the modulus function and onset frequency values increase monotonically with rise in temperature as well as irradiation. This nature of the onset frequency and the relaxation times is in accordance with the conductivity and dielectric constant behavior of irradiated and un-irradiated PPSPN samples.

REFERENCES

1. M. Grossi, B. Riccò, *J. Sens. Sens. Syst.*, 6 (2017) 303–325.
2. J. E. B. Randles, *Discussions of the Faraday Society*, 1 (1947) 11-19.
3. P. Nava, Guzmán, J. Vazquez-Arenas, J. Cardoso, B. Gomez, I. Gonzalez, *Solid State Ionics*, 290 (2016) 98-107.
4. F. Lian, H.-y.Guan, Y. Wen, X.-r. Pan, *Journal of Membrane Science*, 469 (2014) 67–72.
5. T. Itoh, K. Fujita, K. Inoue, H. Iwama, K. Kondoh, T. Uno, M. Kubo, *Electrochimica Acta*, 112 (2013) 221–229.
6. A. S. A. Khair, A. K. Arof, *Ionics*, 16 (2007) 123–129.
7. N. H. Idris, H. B. Senin, A. K. Arof, *Ionics*, 13 (2007) 213–217.
8. A. K. Jonscher, *Nature*, 267 (1977) 673–679.
9. M. Pant, D. K. Kanchan, N. Gondaliya, N, *Mater. Chem. Phys*, 115 (2009) 98–104.
10. A.R. Long, *Advances in Physics*, 31:5 (1982) 553-637.
11. A. Ghosh, *Physical Review: B*, 42:2 (1990) 1388-1393.
12. S. R. Elliot, *Advances in Physics*, 36:2 (1987) 135-217.
13. Ismayil, R. Vasachar, R. F. Bhajantri, P. S. Dhola, S. Ganesh, S, *Nuclear Instruments and Methods in Physics Research B*, 342 (2015) 29-38.
14. A. Kumar, S. Banerjee, M. Deka, (2010a.). *Electron microscopy for understanding swift heavy ion irradiation effects on electroactive polymers*. In: Mendez-Vilaz, A., Diaz, J. (Eds.), *Microscopy: Science, Technology, Applications and Education*. Formatex Research Centre, Spain, pp. 1755–1768.
15. A. Kumar, M. Deka, S. Banerjee, *Solid State Ionics*, 181 (2010b.) 609-615.
16. M. Hema, P. Tamilselvi, *Journal of Physics and Chemistry of Solids*, 96–97 (2016) 42-48.
17. A. Kumar, D. Saikia, F. Singh, D. K. Avasthi, *Solid State Ionics*, 177 (2006) 2575–2579.
18. D. Saikia, A. Kumar, F. Singh, D. K. Avasthi, *Journal of Physics D: Appl. Phys.*, 39 (2006) 4208–4214.
19. R. Arunkumar, R. Babu, M. Usha Rani, S. Rajendran, *Ionics*, 23 (2017) 3097-3109
20. S. Das, A. Ghosh, *Electrochimica Acta*, 171 (2015) 59-65.

21. K. Vignarooban, M. A. K. L. Dissanayake, I. Albinsson, B.-E. Mellander, *Solid State Ionics*, 266 (2014) 25–28.
22. M. Mathew, K. Kesavan, S. Rajendran, *Ionics*, 20 (2014) 439–443.
23. S. Song, J. Wang, J. Tang, R. Muchakayala, R. Ma, *Ionics*, 13 (2017) 213–217
24. G. Kumar, N. Munichandraiah, *Journal of Electroanalytical Chemistry*, 495 (2000) 42-50.
25. H. M. J. C. Pitawala, M. A. L. K. Dissanayake A. A. Senevirante, *Solid State Ionics*, 178 (2007) 885–888.
26. K. M. Diederichsen, H. G. Buss, B. D. McCloskey, *Macromolecules*, 50 (2017) 3832-3841 (2017)
27. S. Ketabi, K. Lian, *Electrochimica Acta*, 154 (2014) 404-412.
28. S. Caimi, A. Klaue, H. Wu, M. Morbidelli, *Nanomaterials*, 8 (2018) 926.
29. S. Choudhary, R. J. Sengwa, *Electrochimica Acta*, 247 (2017) 924–941.
30. N. Gondaliya, D. K. Kanchan, Sharma. P, P. Joge, *Journal of Applied Polymer Science*, 125 (2012) 1513–1520.
31. K. Money, K. Hariharan, J. Swenson, *Solid State Ionics*, 225 (2012) 346–349.
32. Abdullah, S. Z. Abdullah, A. M. M. Ali, T. Winie, M. Z. A. Yahya, R. H. Y. Subban, *Materials Research Innovations*, 13:3 (2009) 255-258.
33. S. Ketabi, K. Lian, *Electrochimica Acta*, 103 (2013) 174-178.
34. P. Sharma, *Study of Conduction Mechanism in PEO-PMMA polymer blend nanocomposite electrolytes*, 2013.
35. S. Ibrahim, S. Mariah, Mohd. Yasin, N. M. Nee, R. Ahmad, Mohd. Rafie, *Solid State Communications*, 152 (2012) 426–434.
36. P. N. Gupta, G. K. Prajapati, *Nuclear Instruments and Methods in Physics Research B*, 267 (2009) 3328-3332.
37. V. Biju, M. A. Khadar, *J. Mater. Sci.*, 38 (2003) 4055-4063.
38. R. Coelho, *Rev. Appl. Phys.*, 18 (1983) 137–146.
39. E. H. Lee, *Nuclear Instruments and Methods in Physics Research B*, 151 (1999) 29-41.
40. R. Kalia, J. K. Sharma, S. Kalia, *Advanced Materials Proceedings*, 3 (2018) 146-150.
41. A. Bobby, N. Shiwakoti, S. Verma, K. Asokan, B. K. Antony, *Physica B*, 489 (2016) 23-27.

42. J. M. Stevels, 1957. In: Flügge, S. (Ed.), *Handbuch der Physik*. Springer, Berlin, pp. 350.
43. D. K. Pradhan, R. N. P. Choudhary, B. K. Samantaray, *International Journal of Electrochemical Science*, 3 (2008) 597-608.
44. G. Hirankumar, N. Mehta, *Heliyon*, 4 (2018) e00992.
45. M. Hodge, K. L. Ngai, C. T. Moynihan, *Journal of Non Crystalline Solids*, 351 (2005) 104-115.
46. P. B. Macedo, C. T. Moynihan, R. Bose, *Physics and Chemistry of Glasses*, 13 (1972) 171-179.
47. N. G. McCrum, B. E. Read, G. Williams, (1991). An elastic and dielectric effects in polymeric solids. Dover, New York.
48. T. Dam, S. N. Tripathy, M. Paluch, S. S. Jena, D. K. Pradhan, *Electrochimica Acta*, 202 (2016) 147-156.
49. S. Raghu, S. Kilarkaje, S. Ganesh, G. K. Nagaraja, H. Devendrappa, *Radiation Physics and Chemistry*, 98 (2014) 124-131.